Superconducting Vortex Noise Measurements on Niobium Films with Periodic Pinning Sites

A DISSERTATION
SUBMITTED TO THE FACULTY OF THE GRADUATE SCHOOL
OF THE UNIVERSITY OF MINNESOTA
BY

Tanner Franz Schulz

IN PARTIAL FULFILLMENT OF THE REQUIREMENTS
FOR THE DEGREE OF
Doctor of Philosophy

E. Dan Dahlberg

September, 2012

Acknowledgements

Isaac Newton once said: If I have seen further, it is by standing on the shoulders of giants. Truly science is a pursuit where all achievements are traced back to the insight of a genius; such a person truly deserves the credit he or she is due. But few of these geniuses are around when you finish taking the GWE, or offer help to practice a presentation, and they don't help you to laugh when you are feeling stressed. I want to thank all of those people who may not have been "giants" when I met them, but from their support alone, I have no doubt that they some day they will be recognized as such.

I want to first thank the Dahlberg lab for the support throughout my research. Hyuk-Jae, and Greg, for welcoming me and helping me get started with my research. Feng Guo, for always offering a helping hand and talking about how we were going to survive till graduation. Dan, Barry and Bern, for volunteering to take over a lab that is changing from an old to a young lab before my eyes. I have no doubt that research will go well for all of you.

Thanks to Dan Dahlberg, for everything you've has done for me as an advisor, you've challenged me to be a better scientist and surprise me with his insight on every project I've worked with him on.

I also want to thank Beth Stadler, and her group for collaborating with me on some unique experiments with superconducting Nb that would become this thesis. Paul Crowell for his help and influence on my research, I can honestly say that I've met few people who work as hard to make a student into a better person. Also thanks to Kurt Wick for numerous conversations that started with physics and led to the real world.

Best regards all the official and unofficial members of office 58, it was great starting graduate school with all of you and I cannot imagine what the past seven years would have been like without knowing all of you.

Thank you to my parents and family, I appreciate your constant thoughts, love and support. And finally, thank you Elizabeth Smith, whom I met over a conversation about why she loved physics and have become convinced that she is possibly the worlds best instructor of happiness.

Dedication

To Mom and Dad,

The lessons you taught me growing up have truely laid the groundwork for everything that I do.

Abstract

Vortex noise in superconductors is due to the motion of quantized flux (vortices) across the surface of the superconductor. This changing magnetic flux gives rise to a voltage which we detect as a noise signal. Previous measurements show that the vortex noise is related to the interaction of the vortices with intrinsic pinning sites which limit vortex motion. These studies show that the noise signal is composed of voltage bursts related to the vortices moving in fits and starts due to the random location and strength of the intrinsic vortex pinning sites. Our samples are composed of a periodic triangular array of holes that serve as vortex pinning sites. These samples show periodic minima in resistance when the vortex/pinning site densities are commensurate. We find a vortex noise signal that is field, current and temperature dependent, arising from the vortices being depinned. We measure the vortex noise to determine if there is a change from uncorrelated vortex depinning below the first matching field where unoccupied pinning sites exist, to highly correlated vortex depinning at the first matching field when the vortexes are commensurate with the pinning lattice. Our measurements show that there is no field dependence in the vortex noise signal, indicating that the vortex depinning is correlated as the lattice is driven by a DC current. We explain this result in terms of the long range order of our pinning lattice and the strength of the vortex-vortex interaction in our 100 nm pinning lattice. Our findings suggest that the vortex noise is dominated by the vortex-vortex not vortex-pinning site interactions.

Contents

List of Figures

Chapter 1

Introduction

- Chapter 2 provides a background into superconductivity, and vortices in superconductors.
- Chapter 3 describes our insulating alumina template and the steps we took to improve our Nb films.
- Chapter 4 describes measurements conducted on our samples which display periodic field response due to vortex pinning.
- Chapter 5 describes the details of our vortex noise measurements on samples at a constant temperature, and constant reduced temperature T/T_c.
- Appendix A describes a vortex simulation that was developed, preliminary tests, and the current state of the program.
- Appendix B is a process recipe that was used to investigate the magnetic phase response of materials under a Magnetic Force Miscroscope.

Chapter 2

Superconductivity Introduction

2.1 Superconductivity Overview

Superconductivity is a phase characterized by two unique properties. The first property is zero electrical resistance, and the second is the expulsion of magnetic flux due to surface currents which persist due to the zero electrical resistance. These two characteristic properties are unique to superconductors and are the basis for the physics we have investigated.

If we consider an infinitely long cylindrical sample in the superconducting state with an applied field directed axially we can observe the stability of the superconductivity state as the field is increased. For low fields the field is expelled from the sample by surface super-currents that extend into the superconductor over a characteristic length known as the penetration depth λ; this is known as the Meissner effect. The cylinder will continue to expel the magnetic field until the field exceeds a critical value H_c where the sample will transition to the normal state.

For samples with a large aspect ratio (cylinders, rods, etc.) the Meissner state is easy to realize if the field is applied along the long axis of the sample. However, for spherical samples the Meissner effect is still present but the magnetic field response is much different. If the sphere were to expel the magnetic flux as in the cylindrical sample then at the edges of the sphere, where the flux collects as it bends around the sample, a large magnetic field would exist for even a small applied field. The magnitude of this flux would quickly exceed H_c and would destroy the superconducting state in

the sphere. In reality we find that spherical superconductors do exist, however, we find that a complete Meissner state does not occur in these samples [1].

To understand why this is the case, consider a thin film with the magnetic field applied perpendicular to the plane of the film. With the perpendicular field applied, the flux penetrates the superconductor and passes through the sample. In order for the flux to penetrate, the superconductor must give up some of its condensate energy, essentially some superconducting order must is lost in order to pass the magnetic field. By sacrificing condensate energy the superconductor creates a normal core, whose diameter is given by the coherence length (ξ). The field will then pass through the normal core; the rest of the superconductor screens the field using a rotating super current over the distance of the penetration length (λ). The magnetic flux is called a vortex due to the circulating current around the normal core. The vortex also represents a quantized flux unit of size $\phi_0 = hc/2e$ where ϕ_0 is the flux quantum h is Boltzmanns constant, c is the speed of light and 2e is the charge of the electrons in the Cooper pair.

The magnetic field response of a superconductor can be put into two different categories either Type I or Type II superconductors. Type I superconductors are characterized by $\xi > \lambda$ and a diamagnetic response proportional to the applied field and a sharply defined critical field H_c above which the sample is normal. Type II superconductors ($\xi < \lambda$) have a diamagnetic response up to a critical field H_{c1} below which there are no vortices. Above H_{c1} the diamagnetic response wanes due to the inclusion of vortices. The sample finally goes normal above a field categorized as H_{c2}, for a type II sample $\xi < \lambda$. Given the demagnetization factor of a thin film to a field perpendicular to the plane, H_{c1} is absent and vortices are always present, and the only critical field is H_{c2} [2]. The field response of Type I and II superconductors can be seen in figure 2.1

Because there is a cost of condensate energy to produce a vortex, it is favorable to place the vortex core in a region where the condensate energy is small. This will causes a vortex core to prefer thinner or dirty regions of the film, where minimal condensate energy is sacrificed to funnel magnetic flux through the sample. The difference in energy between the defect site and the superconducting sample creates an energy barrier that effectively pins the vortex to the defect location.

Vortices in a superconductor, in the absence of any native pinning defects form a triangular lattice known as an Abrikosov lattice as a result of vortex-vortex repulsion

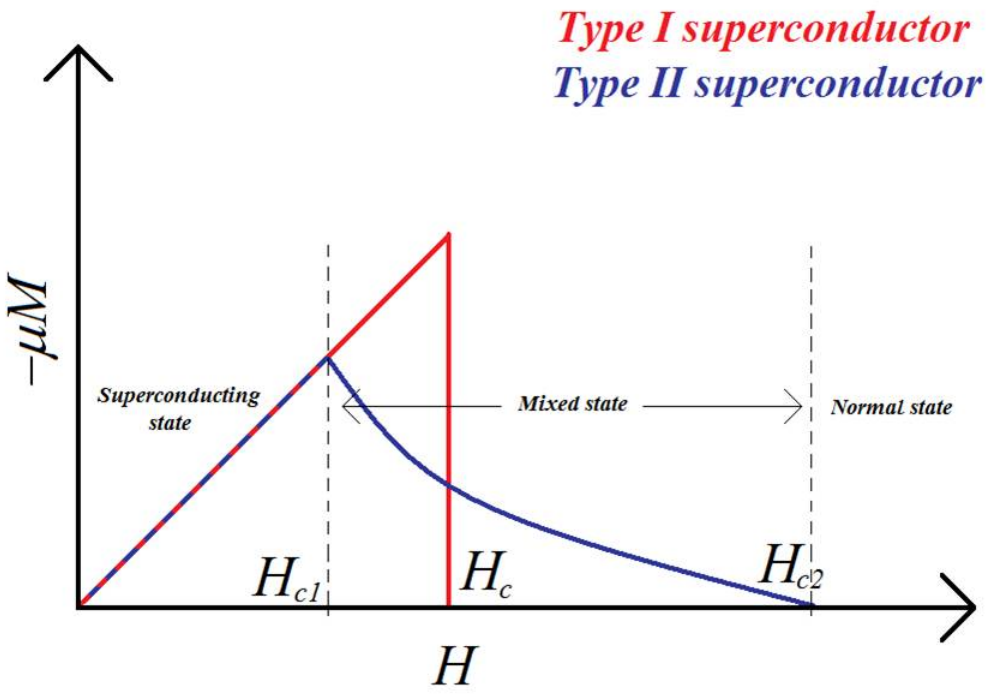

Figure 2.1: Magnetic Field Response of Type I and II Superconductor

Illustrating the difference in critical fields and the effect of vortices on the diamagnetic response of a superconductor

as shown in figure 2.2. The number of vortices and therefore the spacing of the vortex lattice is set by the applied field. We can calculate the vortex density in a thin superconducting film by simple dimensional analysis. Given an applied field H we expect a vortex lattice spacing $a = (\phi_0/H)^{\frac{1}{2}}$; due to the triangular geometry there is a numerical prefactor of 1.075.

2.2 Current vortex interactions

If we consider a superconducting film exposed to a perpendicular applied field there will be vortices which penetrate the film at a density proportional to the applied field. In

the absence of any pinning sites the vortices will be in a triangular lattice. An in plane current causes a Lorentz force ($\vec{F}_{Lorentz} \simeq q\vec{v} \times \vec{B}$) which will accelerate the vortices in a direction perpendicular to the applied current and field.

By Lenzs law we know that a changing magnetic flux produces a voltage; $EMF = d\phi/dt = n\phi_0 dx/dt$ where n is the number of vortices in the film. Thus a voltage results from the vortex motion along the current direction, which means the superconductor effectively becomes resistive. The dissipative response of the vortices continues until the sample is driven out of the superconducting state by exceeding either the critical current $I_c(H)$ or critical field. Thus we find that the EMF generated by moving vortices should grow as a function of applied current or field [1].

Vortex motion may be mitigated by the use of defects which pin the vortices; the defects may be intrinsic or artificial, or a combination of both. Essentially a vortex is pinned by any feature which reduces the condensate energy, i.e. the normal core costs less energy in this region. By engineering defects such as holes in the superconductor, vortices can be pinned, this reduces the vortex motion. Using lithography techniques it is possible to produce very regular, periodic pinning sites. Since vortices prefer to sit in a pinning site a periodic lattice provide sites which fill with increasing applied field; at some field the vortex density is commensurate with the pinning site density [4]. At this matching field (H_1), vortex motion is greatly suppressed which significantly reduces the measured effective resistance, see figure 2.3.

This behavior has been experimentally investigated in many systems and geometries which include work on Josephson junction SNAP networks, physical defects caused by magnetic structures [5, 6, 7, 8], radiation damage [4], and variations in superconducting order due to underlying topography corrugations [9, 10, 11, 12, 13]. Extensive calculations and simulations have been conducted also and show a wide range of transport properties under the influence of a driving force from the applied current [14, 15, 16, 17, 18, 19, 20, 21].

Here we present our results investigating the effects of vortex pinning by a triangular array of 60 nm anti-dots (holes). We also include our studies of the vortex noise produced by a sample as the field changes under the influence of a DC applied current Chapter 5.

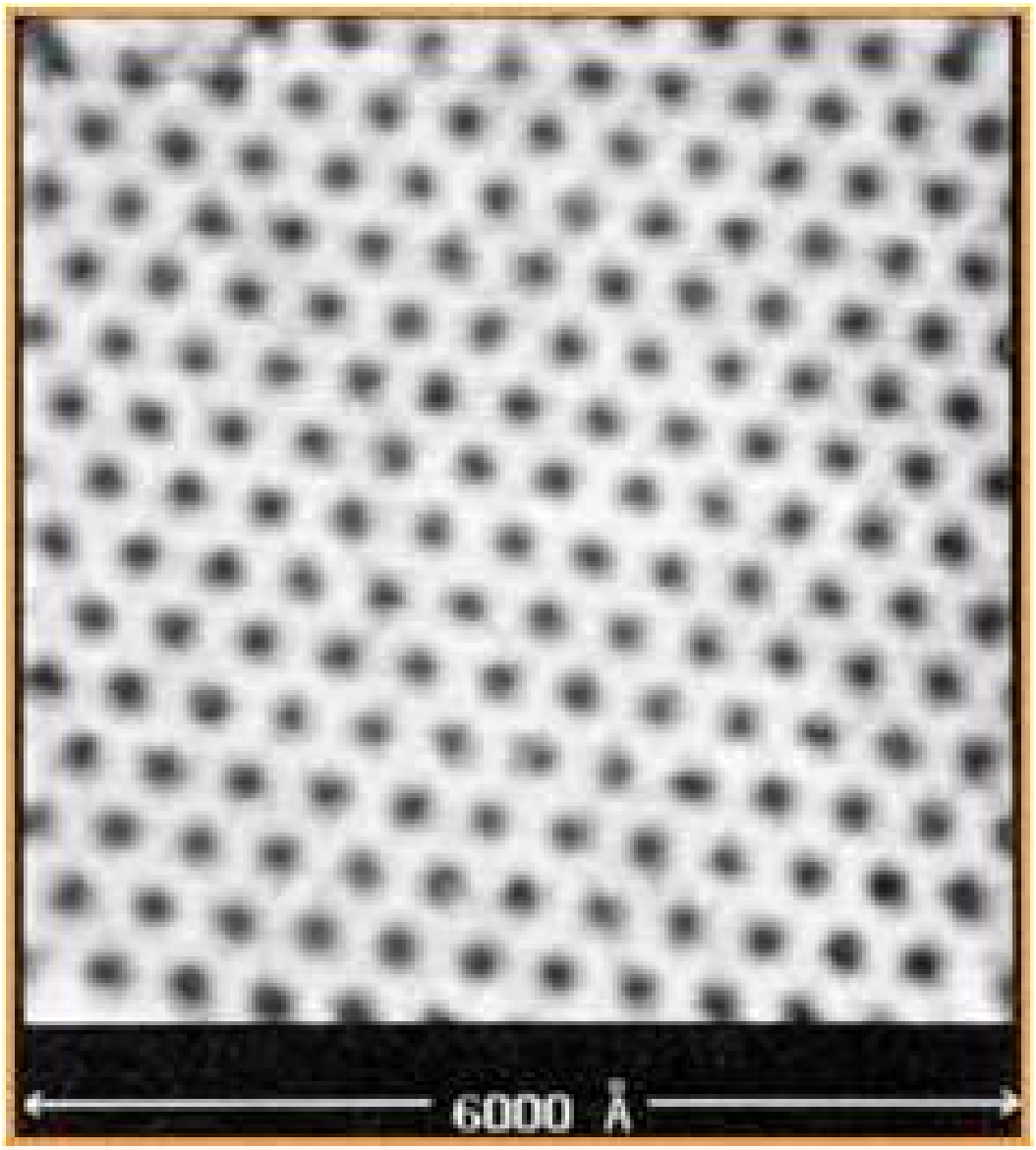

Figure 2.2: Abrikosov Lattice

STM image of an Abrikosov lattice in a $NbSe_2$ sample at 1.8 K with a applied field of 1 T. Sample is very clean and has no artificail pinning sites, dark dots represent the normal core of the ordered vortex lattice [3].

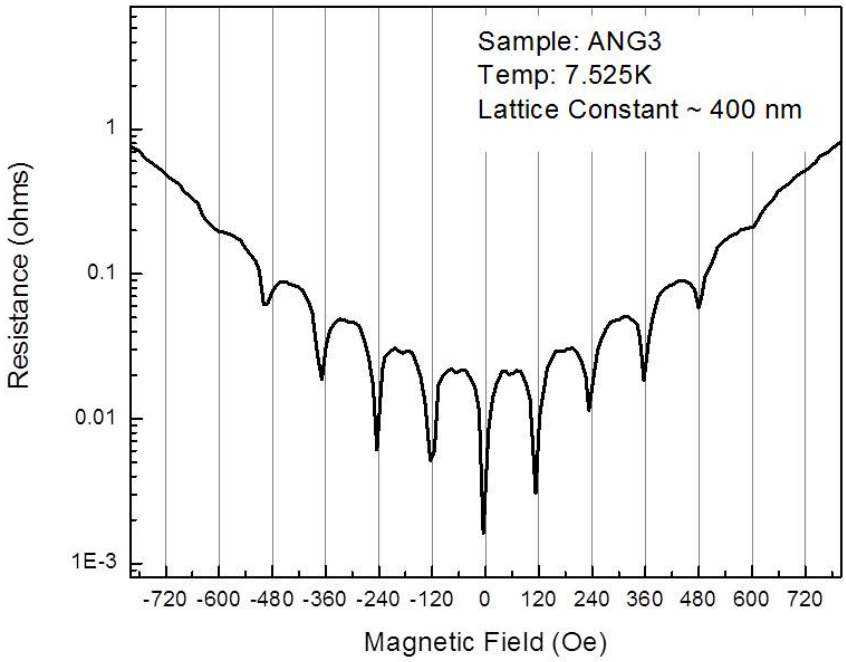

Figure 2.3: Magnetoresistance of a 400 nm square array

Resistance vs. Applied field for a sample with a 400 nm square array of Co dots. Resistance minima correspond to the vortex density matching the artificial pinning site density.

Chapter 3

Aluminum Oxide Anti-dot Templates

We deposit superconducting Nb thin films on an insulating Al_2O_3 substrate that has a periodic triangular array of anti-dots. The anti-dots are the result of a controlled anodization where pores are etched into an aluminum foil during anodization. It has been shown that by adjusting the anodization current and voltage, the size and spacing of these pores may be controlled. Thus, the anodization of aluminum can be regarded as a self-organized process that changes a conductive aluminum foil into an insulating Al_2O_3 surface perforated by regularly sized holes.

Minimizing the defects in the anti-dot lattice can be accomplished by nano-imprinting, or anodizing multiple times to fabricate highly periodic triangular arrays of anti-dots. Our alumina templates are fabricated using a two-step anodization process. The first anodization defines pilot holes which start randomly but order themselves as the pores channel deeper into the film the complete process is described in detail elsewhere [13]. In brief, after the first anodization step the anodized alumina layer is removed revealing an aluminum surface dimpled by shallow regularly spaced pores. The pores serve as a guide for the second anodization which deepens the pores, resulting in an array of equally sized and spaced anti-dots in a triangular array. Once again, the lattice parameters are controlled via the anodization current and voltage.

Atomic force microscope (AFM) scans of our substrates show a triangular anti-dot

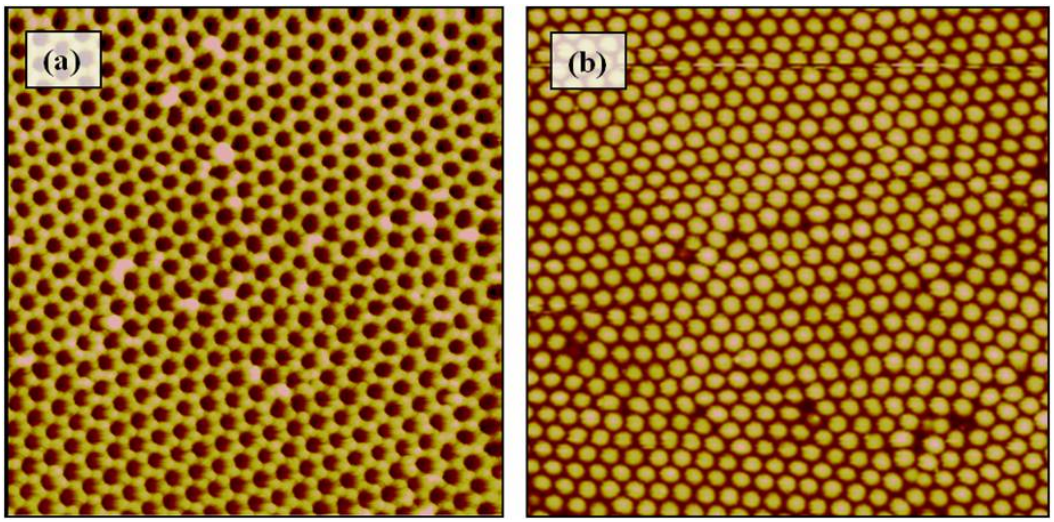

Figure 3.1: 2x2 micron AFM scans of the aluminum oxide template.

Scans show that each side of the template has a different surface morphology. The majority of our samples were Nb films deposited on the anti-dot surface (a), where the dark regions represent 60 nm pores that can trap a superconducting vortex. While the corrugated dot surface (b) also displays weak matching effects at the intersection of the trench between neighboring dots due to variations in Nb thickness from the dots.

lattice with a lattice constant of 100 nm. The pores are typically 60 nm in diameter, with 40 nm bridges between pores. A representative 2×2 micron surface scan is shown in 3.1. Surface characterization show that the long-range order in our substrate is polycrystalline consisting of triangular lattice crystallites approximately a $micron^2$ in area. Additional surface measurements made using a scanning electron microscope, verify the polycrystalline nature of the alumina template (figure 3.3).

We have investigated the long range order by taking 2-D Fourier transforms of the sample surface. Due to the six fold symmetry of our anti-dot lattice we expect the Fourier transform to show six distinct dots at the corners of a hexagon. For surface scans over an area larger than a micron, the transform shows a ring with six blurred groupings indicating that the sample is polycrystalline at lengths above a micron (see Figure 3.2). Six well resolved points are found for surface scans up to a micron. This, as well as our surface scans, is evidence of a well ordered triangular anti-dot lattice

on length scales up to a micron. Since the lattice constant is $\sim$ 100 nm each ordered crystallite contains over a hundred well-ordered pores.

While one side of the alumina substrate shows a triangular anti-dot lattice the opposite side of the substrate corresponds to a triangular dot lattice. The size and order of the dot lattice is comparable to the anti-dot lattice. The dot lattice introduces thickness variations in the superconducting film and produces similar vortex matching effects as the anti-dot lattice, however, the pinning geometry is now hexagonal not triangular. Six samples have been made using the dot lattice and will be addressed in the chapter 4 (see figure 3.1B).

3.1 Sample Fabrication

The samples consisted of a 100 nm niobium film sputtered on top of the alumina template. While the deposition is straightforward a considerable amount of work has been conducted to ensure that the film has a high critical temperature (T_c) and a sharp normal/superconducting transition. With improvements to our deposition procedure, we have been able to achieve critical temperatures in the range of 7-8 K, still far from the book value of bulk Nb 9.5 K. However, a T_c above 7 K, is comparable to or above the Nb T_c of similar artificial pinning experiments [5, 11].

3.2 Nb Deposition Procedure

The following steps are presented as a means to recreate the high T_c Nb in our deposition chambers, however, further refinements may still be possible. Most of the Nb samples were magnetron sputtered in the small deposition chamber. The Nb target is a high purity sample (2.5 x 0.25 inch 99.98% Nb) from AJA International Inc. This target produces films with a superconducting transition temperature up to 2 K higher than the previous Nb target which had a purity of 99.95%.

To minimize the influence of contaminants from outside sources or magnetic particles only non-magnetic materials have been used in the small deposition chamber. Further, the surfaces of the chamber have been cleaned extensively to minimize the influence of possible contaminants [22]. The RGA spectrum shown in (figure 3.4) shows the

components of the base pressure in our system before and after pre-sputtering. We use an aggressive pre-sputter of Nb, (which also acts as a getter) by sputtering at a power of 250 W, 3.0 mTorr Ar, for 25 min while the sample is protected by a shutter. This lowers the chamber pressure to $\sim 1.0E-8$ Torr 24 hours after presputter. This is the pressure at which the samples are deposited at a power of 40 W with 3.0 mTorr Ar, resulting in a deposition rate of 0.8 angstrom/sec.

A witness sample is made simultaneously with our alumina samples; this allows a comparison of T_c and a thickness measurement. In general, witness samples show an improved T_c compared to alumina template samples deposited at the same time. The witness samples consist of a wire $20\mu m$ wide, defined by conventional lithography on a SiNx substrate, whereas the alumina template is affixed to a supporting substrate of SiNx using either GE varnish or rubber cement. Alumina template samples, prior to summer 2010, had minimal surface cleaning and show a broad normal/superconducting transition (width of up to 1 K). A cleaning process was employed where the alumina is put through a three solvent wash of Acetone, Methanol and Isopropanol alcohol respectively. With the solvent wash, the transition temperature is much sharper (width 0.05 K) as shown in (figure 3.5). This implies contamination from the surface of the alumina template is a large factor in the reduction of the Nb film quality.

The best base pressure, in the small chamber, was achieved by letting the system pump down from atmosphere for at least a week. Water vapor was removed by using a heating strip around the base of the chamber. Viton O-rings on the chamber ultimately limit the temperature the system can be exposed to, thus baking out the system was done by alternating 12 hours on 12 hours off for several days. While this step may be overly cautious, the local temperature at the O-ring is difficult to measure and this process favors the side of caution. Once the chamber has been baked out the ultimate base pressure should be at the low $3E-8$ Torr (winter) $4E-8$ Torr (summer).

The samples were defined either by using a shadow mask or using a conventional lift-off lithography. We found that for lithographic processing, the alumina templates could be attached to a 2.5 cm square backing Si substrate using mounting wax. The mounting wax is fairly resistant to solvents and provides a means to move a sample from deposition to measurement simply by heating the substrate thereby minimizing the strain applied to the fragile alumina template.

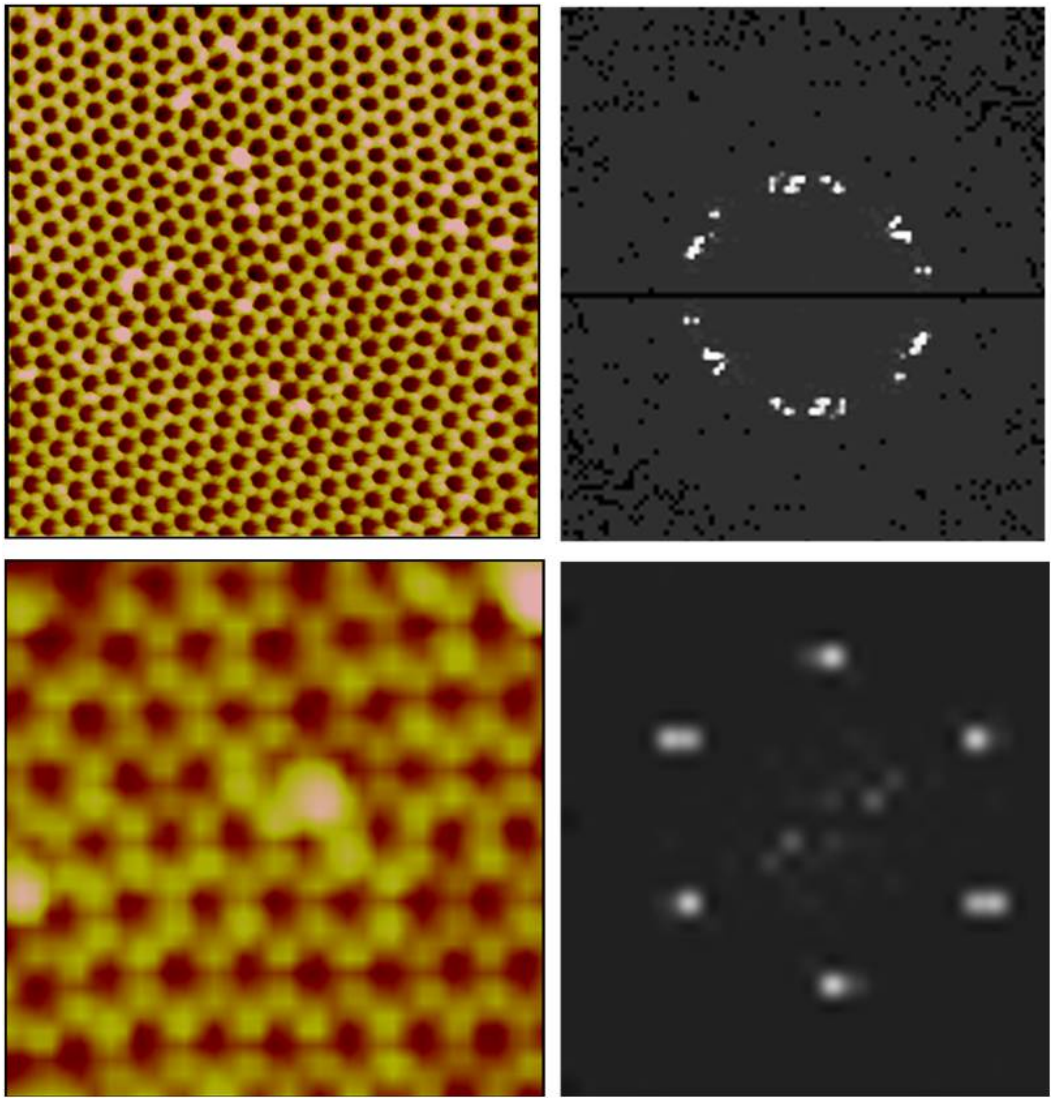

Figure 3.2: Fourier transform of the anti-dot template surface.

Left images show the topography scan. While right images show the Fourier transform (FT) of the topography image. The top left image is a $2\mu m^2$ scan and shows several anti-dot crystallites intersecting and disrupting the triangular order. The corresponding FT shows six smeared out regions. The bottom left image is a $0.8\mu m$ scan showing a very periodic order, the FT shows six well resolved points. Similar scans from our samples verify that order extends up to $\sim 1\mu m$ for our 100 nm lattice constant films.

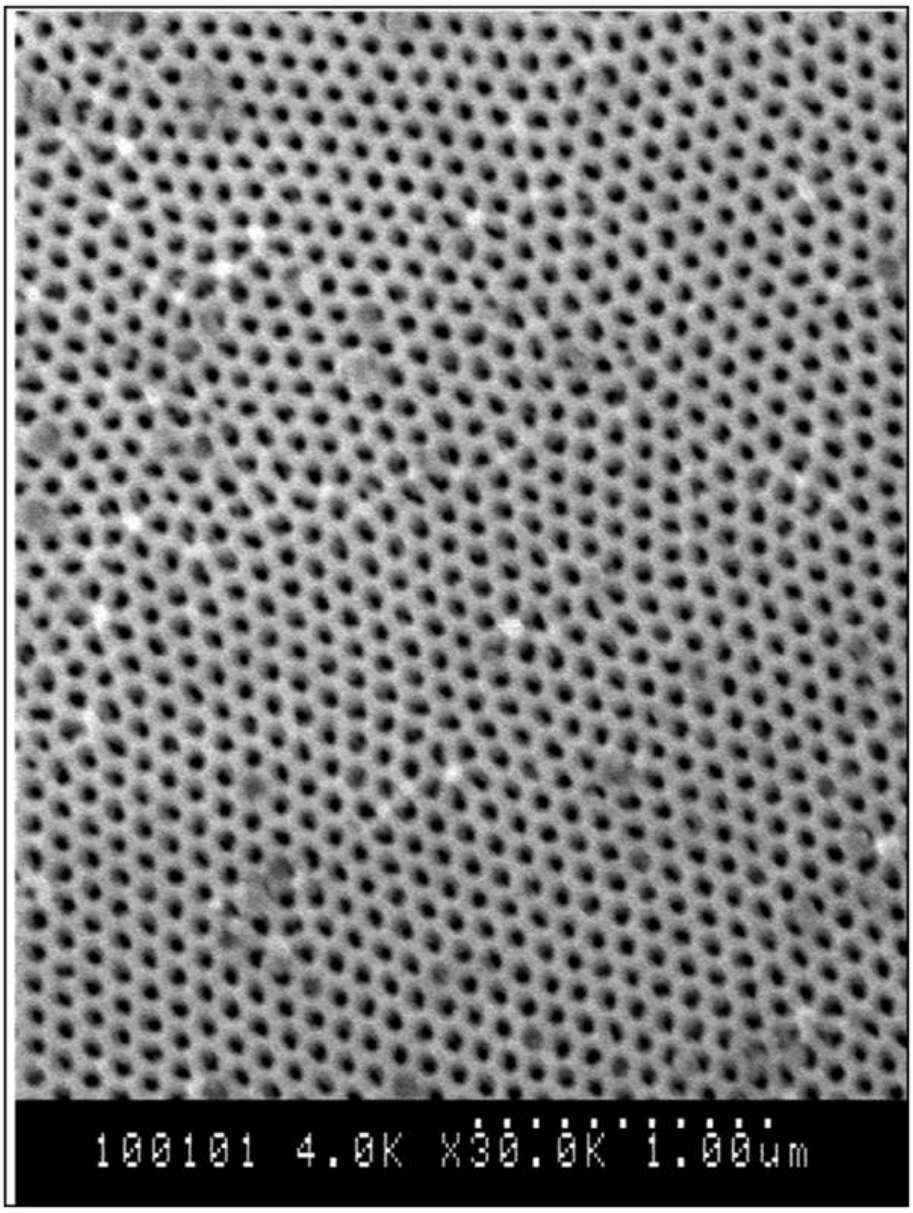

Figure 3.3: SEM image of the alumina template with 100 nm of Nb.

We see the periodic 60 nm anti-dot lattice is present after the Nb is deposited on the template. We observe that in our samples the Nb film covers the surface of the template and is perforated by a regular triangular lattice of anti-dots.

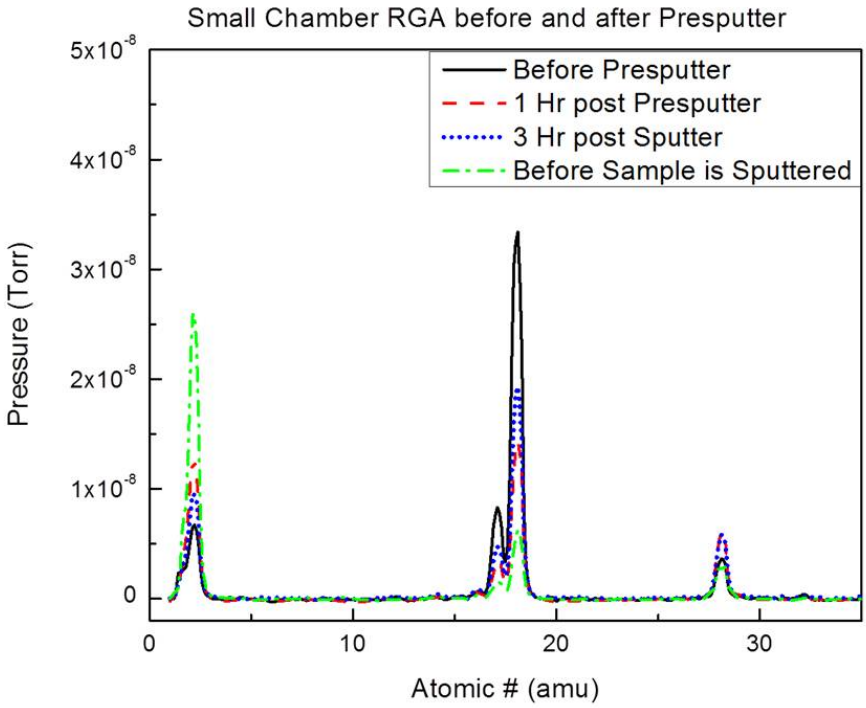

Figure 3.4: RGA scan of deposition chamber prior to Nb deposition

The plot shows how the pre-sputtered Nb acts as a getter, effectively lowering the partial pressure for O_2 (16 amu), and H_2O (18 amu). Contamination due to O_2 is shown to lower the T_c of Nb significantly[22].

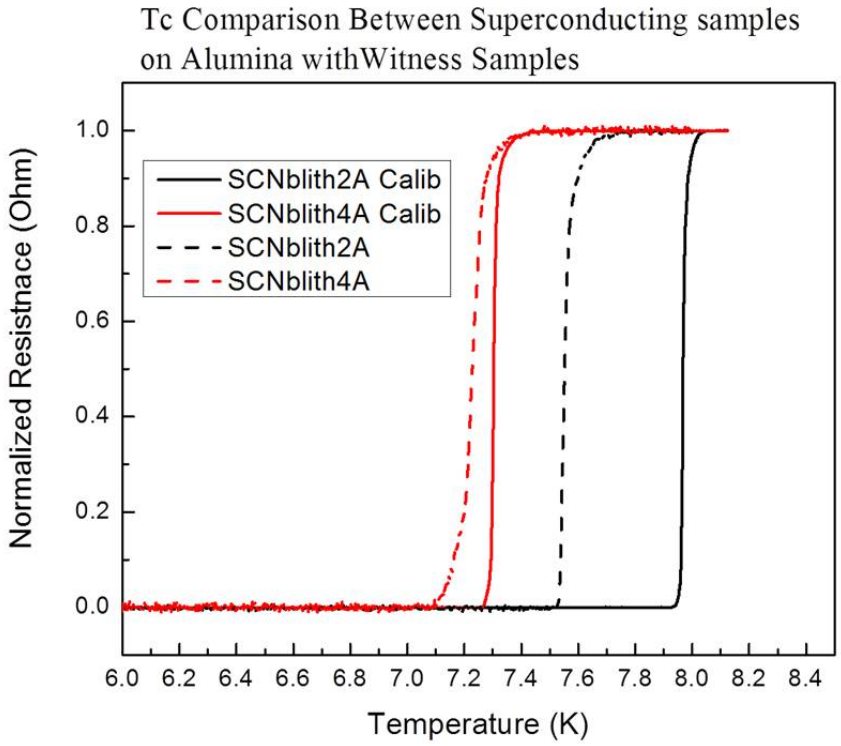

Figure 3.5: R vs. T comparison

Figure compares the T_c for superconducting Nb deposited on alumina anti-dot templates to Nb deposited on a SiNx witness substrate. While the T_c for films deposited on the alumina templates is slightly depressed, the T_c and transition width of the template samples are comparable to the witness films.

Chapter 4

Vortex Pinning/Lattice Matching Measurements

Measurements of the samples resistance, critical current, magnetization, and transition temperature show a periodic response as a function of applied field. The periodic field dependence is a result of the artificial pinning lattice in our films. For measurements on the anti-dot pinning lattice, the first peak coincides with a vortex density that is commensurate with our lattice spacing, and higher matching effects are observed at integer multiples of the first matching field. The matching fields for our triangular anti-dot array can be calculated by using

$$H_m = 1.075(\frac{\phi_0}{a^2})m \tag{4.1}$$

where a is the lattice constant of our pinning sites, ϕ_0 is the flux quantum and m is an integer. For our artificial pinning array with a lattice constant of 100 nm as measured by AFM and SEM, we calculate a first matching field $H_1 = 2220$ Oe. In general, a pinning site can hold more than one vortex present. The occupation number, n_s, is a function of the superconducting coherence length $\xi(T)$ and the pinning site diameter d and is given by [23, 24, 25]

$$n_s = \frac{d}{4\xi(T)}. \tag{4.2}$$

For our samples an AFM scans show an anti-dot diameter of $\sim$ 60 nm, and from

Little-Parks like experiments the temperature coherence length, $\xi(0) \sim 18$ nm. This gives an n_s of 0.79, which means that the holes will be singly occupied. Higher matching fields e.g. H_2, H_3, would then result from interstitial vortex pinning. From previous experiments and simulations, it has been shown that the first commensurate pinning is much stronger than interstitial vortex pinning [20, 26].

We have conducted a variety of vortex matching experiments on over 20 samples to investigate our Nb films on an alumina anti-dot template. The experiments include transport measurements (critical current, voltage, or resistance versus field) and measurements of the superconducting film transition temperature and magnetization versus field. All measurements show periodic behavior as a function of applied field. Due to the variation in sample quality over the course of our measurements, we have found that some experiments are better suited to specific sample properties (broad/narrow transition temperature, high/low T_c).

What follows are descriptions of the experiments we have conducted on our films along with the experimental setup, representative data plots, a summary of the measured samples and some measurement considerations.

4.1 Resistance vs. Field Measurements

We start with measurements of the resistance as a function of field. The samples were measured either in a liquid helium cryostat or a Quantum Design Physical Property Measurement System (PPMS). In both cases the magnetic field was oriented perpendicular to the film plane. In general, the measurement temperature was adjusted to be slightly below the transition temperature. Four-terminal measurements were made of a sample's voltage using a resistance bridge as the applied field was slowly swept (≤ 11 Oe/sec).

Data was taken at a fixed applied current; increasing the current resulted in an increase in voltage across the sample driving the sample normal at a lower applied field due to an increase in vortex motion. Plots of the resistance vs. applied field are shown in (figure 4.1 and 4.2), we observe a resistance minimum at the matching field of 2250 Oe. This 1% difference between our calculated $H_1 = 2220$ Oe corresponds to a lattice constant of 99 nm well within the uncertainty of the 100 nm lattice constant from AFM

measurements. Weaker inflection points are observed at integer multiples of H_1, indicate the weaker pinning effects at the interstitial matching fields.

The data in the V vs. B measurements corresponds to the signal generated by vortex motion. Vortex pinning strength grows inversely with sample temperature below T_c [1, 6, 27], we find that for temperatures far below T_c matching effects are indiscernible (V=0). Thus, V vs. B measurements must be taken while the sample is in a mixed state with mobile vortices, this situation is easily achieved by measurements either very close to T_c ($> 90\%T_c$). Or by biasing a sample with a larger driving current which depins vortices at lower temperatures $< 90\%T_c$, this behavior is shown in (figure 4.1).

Due to the 100 nm lattice spacing of our pinning array the matching effects occur at a period of ~ 0.25 Tesla. Which requires large applied fields (comparable to H_c) to observe several matching fields. We have found that such a field range only exists in samples with a broad normal to superconducting transition. While it is easy to keep the sample in the superconducting state by lowering the measurement temperature, voltage variations at low temperatures are below the detectior resolution. Therefore, we find that the convenience of V vs. B measurements comes at the cost of measuring very dirty superconducting samples.

The V vs. B measurements, which must be made very close to T_c, have an added complication due to the transition temperature changing with applied field. Superconducting witness films which have no artificial pinning sites, show that T_c decreases proportional to the applied field. Since a measurable voltage can only be recorded in the mixed state region, we find that samples with a broad transition (> 0.5 K width) offer a wide range of applied fields (> 5 kOe) where the sample is between the superconducting/normal states and will display field matching effects. Samples with a sharply defined transition temperature (~ 0.05 K width) provide a much narrower field range where the sample is between the superconducting/normal states (~ 1 kOe). (Figure 4.3) shows the different transition edges measured in our experiments, with the broad edge corresponding to a sample with an V vs. B signal that is easy to measure.

The effects of a broad transition versus a sharp transition can be seen in the contour plot in figure 4.4. Here a sample with a broad superconducting transition is show in the upper figure. We see that if we pick a temperature 5.5 K we see that the mixed state (rainbow colored region) extends several thousand Oe, and would be a good sample to

measure the V vs. B on, as we can observe from see figure 4.1. Whereas the sample shown in the bottom of figure 4.4 has a very narrow transition region for any applied field, and serves as a poor sample to measure V vs. B on, as we observe in figure 4.2 which shows only a single matching field before transitioning normal.

4.2 Magnetization vs. Applied Field

It is possible to expand the region where matching effects may be observed with magnetization measurements. Magnetization measurements have been utilized in a variety of periodic pinning lattice measurements [20, 10, 26] which make use of a low temperature VSM to measure the diamagnetic response of the sample as a function of applied field. It should be noted that these measurements can be conducted without a current. While we have measured the magnetization of only five samples, it is an option that offers some unique benefits compared to standard transport measurements.

Measurements employed a Quantum Design MPMS SQUID magnetometer with the magnetic field applied perpendicular to the surface of our sample. The magnetic field was stepped in 50-100 Oe increments from a positive field ($> H_{c2}$) to negative fields and back to a large positive field; this provides a hysteresis loop of the samples magnetic response. A roughly diamond like response is observed below T_c as seen in figures 4.5 and 4.6 indicative of the diamagnetic response of the superconducting Nb. The largest diamagnetic response occurs close to zero applied field where no vortices are expected. Due to the periodic pinning lattice in our samples, local maxima appear at the matching field where the vortex density matches the pinning density. The diamagnetic response is suppressed as interstitial vortices enter the sample for fields above the matching field. At high fields the applied field exceeds H_{c2} killing the diamagnetic response once the sample is in the normal state.

Vortex pinning and diamagnetic response are roughly inversely proportional to the sample temperature [1]. Thus, the diamagnetic response is observed to grow with decreasing temperature as seen in figure 4.6.

We measured the diamagnetic response of several films, but have not performed transport, or noise measurements with them. However, local noise measurements might be ideally suited to the SQUID if small Josephson junctions could be employed as local

pick-up coils to measure vortex motion in the sample [28, 29, 30, 31]. Difficulties with the SQUID measurements are ensuring the sample is held stationary and perpendicular to the applied field in the sample holder. Other problems consist of measuring T_c as the diamagnetic signal grows only below T_c, and insuring the measurements are conducted below T_c, and distinguishing the diamagnetic response of the Nb film from the substrate at temperatures close to T_c. While the above factors have made our measurements challenging, we are still able to see reasonably well resolved matching effects comparable to previous magnetization measurements on a periodic pinning lattice [10].

4.3 Critical Current vs. Applied Field

Measurements of a samples critical current are conducted by establishing a voltage/resistance threshold (typically half of the normal state resistance (R_N)); measurements are four-terminal. A DC current is systematically stepping while measuring the corresponding voltage/resistance across the sample at a specific applied field. Samples are held at a fixed temperature below T_c while stepping the current in $5 - 10\mu A$ steps. At each applied field a measurement of the voltage vs. current response (VI) is recorded. This process is repeated making sure to capture the complete superconducting to normal transition. By comparing the VI measurements at different applied fields (Figure 4.7) the field dependent characteristic current $I_c(H)$ can be plotted for each applied field; plots of I_c vs. applied field show local maxima in I_c when the applied field is a multiple of H_1.

Our critical current is temperature dependent since vortex pinning grows as the sample temperature is lowered. Thus I_c grows as the temperature falls below T_c. Our I_c measurements are conducted at a temperature close to T_c, and with a small current step size ($5 - 10\mu A$) such that each IV plot shows a continuous voltage evolution. Care is taken to avoid heating. Measurements with larger current steps may mask the effect of I_c at different fields as the critical current changes by several μA for each applied field step. Representative plots of I_c vs. applied field are shown in figure 4.7. Here we find a samples I_c corresponds to a current density of $8000 A/cm^2$ similar to previous measurements of I_c in sample's with a periodic pinning array [5].

Measurements of the critical current provide a direct measure of the response of

the vortices to the periodic pinning array in a sample. Further, there are numerous theoretical calculations of the pinning strength, and vortex flow dynamics associated with measurements of the voltage/current characteristics [20, 32, 21].

4.4 Transition Temperature vs. Applied Field

Perhaps the most useful measurement we have conducted on our superconducting samples with periodic pinning is a measurement of the transition temperature vs. applied field. It is a measurement that works for samples with both wide and narrow superconducting transitions at a fixed current. This is especially useful for films with relatively large matching fields ($>$ 2 kOe) where capturing multiple matching effects at a fixed temperature is difficult to achieve. These measurements also allow a determination of a samples coherence length $\xi(T)$, electron mean free path l, and a mapping of a samples $H_{c2}(T)$ which is useful when conducting measurements of vortex noise.

Our analysis follows from previous temperature experiments on superconductors with an artificial pinning lattice [10, 11]. We measure the voltage across a sample at a fixed current as the temperature is slowly swept across the transition temperature. This process is repeated at different fields observing how the transition temperature changes with field. When the axes of the anti-dots are parallel to the applied field, the magnetic flux passes through the holes and thus is comparable to a Little-Parks measurement [1, 27]. The Little-Parks experiment can be understood by considering the kinetic energy of the electrons. At temperatures close to the superconducting-normal transition the kinetic energy of electrons must be identical below and above T_c. The effect of an applied magnetic field increases the kinetic energy of the electrons while the flux captured by a pore suppresses electron motion. Thus when all the pores contain an integer flux quantum there is a maximum suppression of vortex motion and a local maximum in T_c (Figure 4.8).

The critical field $H_{c2}(T)$ varies as [11]:

$$H_{c2}(T) = \frac{(12)^{1/2}\,\phi_0}{2\pi w \xi(T)} \tag{4.3}$$

where w is the width of the bridge between adjacent pores ($\sim$ 40 nm for our films), ϕ_0 is the flux quantum, and $\xi(T)$ is the temperature dependent coherence length given

by:

$$\xi(T) = \xi(0)\left(1 - \frac{T}{T_c}\right)^{-1/2} \tag{4.4}$$

where $\xi(0)$ is the coherence length at $T = 0$, and T_c is the transition temperature with zero applied field. We can rewrite the equation for $H_{c2}(T)$ in terms of $\xi(T)$ as:

$$\frac{(12)^{1/2}\,\phi_0}{2\pi w H_{c2}(T)} = \xi(0)\left(1 - \frac{T}{T_c}\right)^{1/2} \tag{4.5}$$

Solving this equation for T (only free parameter is $\xi(0)$)

$$T = T_c(1 - (\frac{2\pi w H_{c2}(T)\xi(0)}{(12)^{1/2}\,\phi_0})^2) \tag{4.6}$$

Fitting our data to this expression gives a $\xi(0) \lesssim 18$ nm for most films, indicating we are in the dirty limit for all our samples (Figure 4.8).

Once $\xi(0)$ is found we can also calculate the electron mean free path by using $l = 1.38(\xi(0)/\xi_0)$ [1] where $\xi_0 = 38$ nm is the book value of the Nb coherence length; calculations of the electron mean free path are found to be in the range of 10-12 nm.

Calculating $\xi(0)$ gives an independent measure of the superconductor quality. This can be illustrated by comparing two different samples with very different coherence lengths. The samples are SCNb4A and SCNblith2A the respective coherence length of each sample is ~ 9 nm and 18 nm. Sample SCNb4A has a broad resistive transition (~ 1 K) with a T_c of 5.3 K while SCNblith2A has a very sharp transition (< 0.1 K) and a T_c of 7.5 K (Figure 4.3). Calculating the vortex saturation number n_s for a pore diameter of 60 nm gives $n_s = 1.7$ for SCNb4A and $n_s = 0.75$ for SCNblith2A, thus each pore or antidote in sample SCNb4A can hold almost two vortices in the 60 nm anti-dot sites [25].

Looking at plots of T_c vs. B for each film we see that SCNb4A shows multiple strong matching features while SCNblith2A shows a single strong peak while higher matching effects appear as weaker inflection points. A samples coherence length ultimately determines the highest vortex density the sample can hold, thus SCNb4A with a smaller coherence length is more likely to fit multiple vortices in each pinning site and the interstitial region leading to more than three matching fields as can be seen in figures 4.1, 4.7 and 4.8.

While the increased matching fields illustrate the effects of our periodic pinning array, we have tried to increase the coherence length and transition temperature of our Nb films. In this way we have tried to improve our film quality/decrease intrinsic vortex pinning sites (see for example the transition temperature T_c figure 4.3) at the cost of only a single commensurate field and at most two interstitial matching fields e.g. figures 4.2, 4.4 and 4.2.

4.5 Alumina Template Backside Measurements

Previous measurements on alumina templates made in a manner similar to ours show that both the top and bottom template surfaces have periodic topographies that can trap superconducting vortices [26]. While AFM surface scans are done on all samples to ensure that our Nb film is deposited on the anti-dot surface of the template, we have made five samples using the domed backside of the template. Here vortex pinning occurs at the corners of a hexagonal lattice from thickness variations in the Nb film caused by the domed surface.

While the matching field for the hexagonal lattice is similar to the triangular antidote lattice, it is not the same. The second matching field for the triangular lattice corresponds to the first matching field for the hexagonal lattice. The first dip in MR measurements on the hexagonal films correspond to a half filled hexagonal lattice $H_{1/2}$, and the first interstitial matching field corresponds to $H_{3/2}$ as shown in figure 4.10. Thus the backside, allows a measurement of two commensurate pinning fields, compared to the single commensurate field for the triangular lattice.

Film thickness is crucial on the backside measurements, we found that it was easy to deposit too much Nb and produce a film that exceeds the variation due to the domes ($\sim$ 50 nm). Our measurements could only resolve the $H_{1/2}$ peak and little else, still the backside measurements provide an additional means to differentiate between commensurate and interstitial vortex pinning.

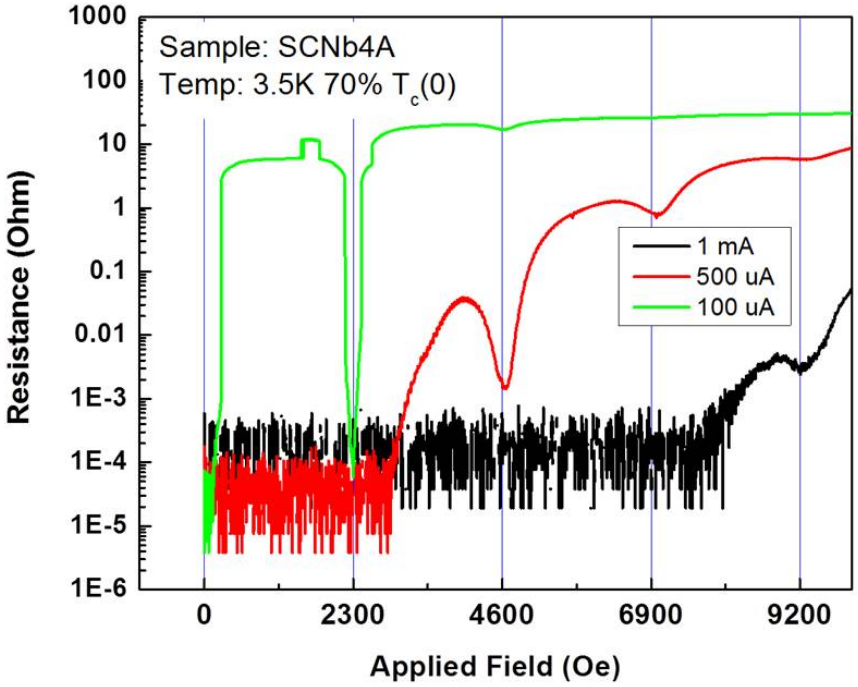

Figure 4.1: Magnetoresistance of a periodic anti-dot lattice.

Matching effects at multiples of 2300 Oe correspond to commensurate and interstitial pinning of the vortex lattice by the anti-dot artificial pinning array. The sample had a broad transition and a low $\xi_0 \sim 9$ nm. Changing the current in the sample depins more vortices and suppresses matching effects.

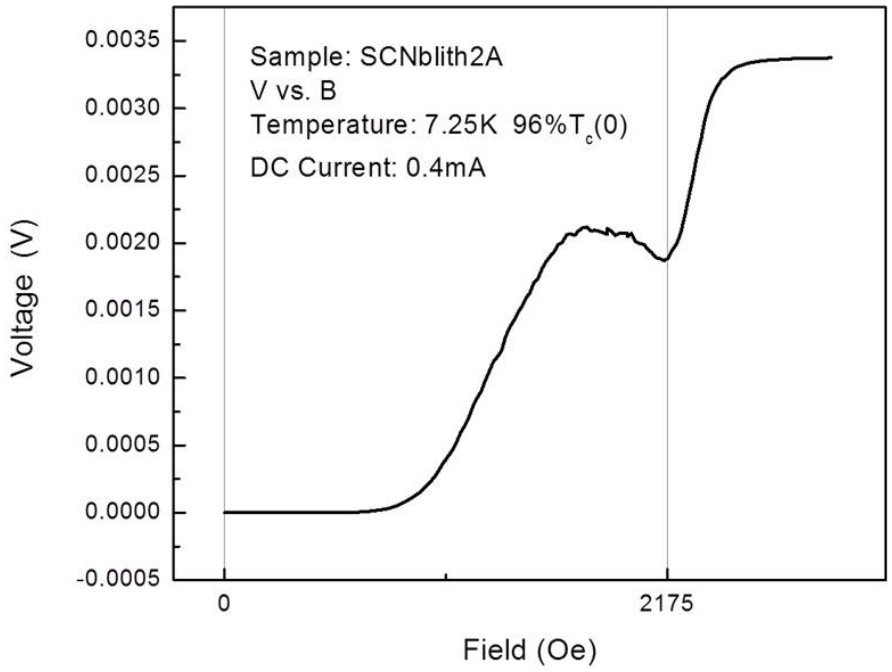

Figure 4.2: Magnetoresistance of a sample with a sharp temperature transition

This sample had a very sharp temperature transition (~ 0.05 K in width), and $\xi_0 \sim 18$ nm. Because of this, it is difficult to resolve multiple MR matching effects. The above peak is due to commensurate matching of the vortex lattice to the artificial pinning site lattice.

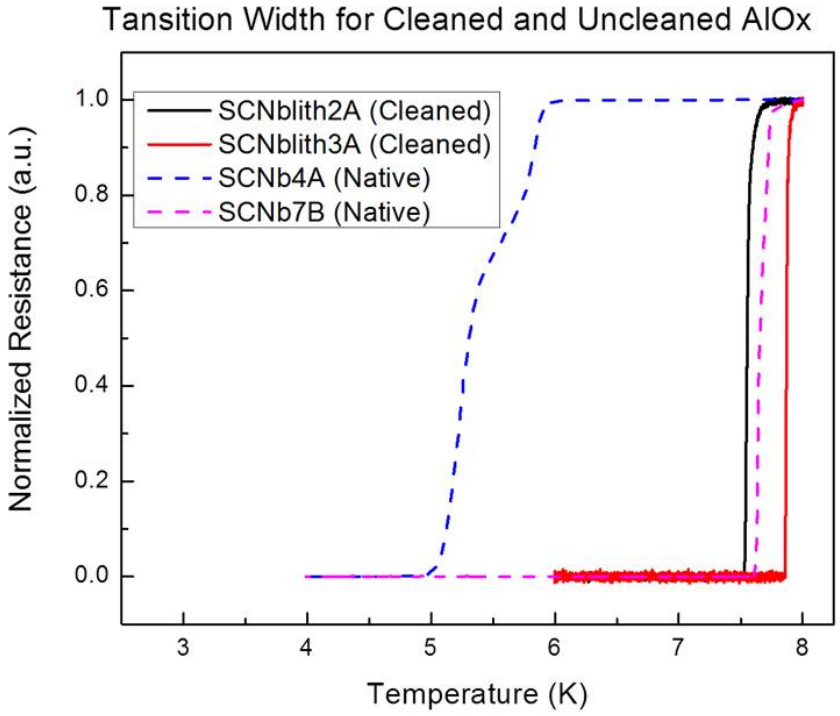

Figure 4.3: Normalized R vs. T for native and cleaned templates

Four different Nb films on alumina templates showing how both sample T_c and transition width have changed as deposition process has been improved. Dashed lines illustrate oldest samples and show a wide variability in sample T_c as well as a broad transition region. Samples cleaned with a solvent wash show a consistent $T_c > 7$ K and have a much sharper transition width.

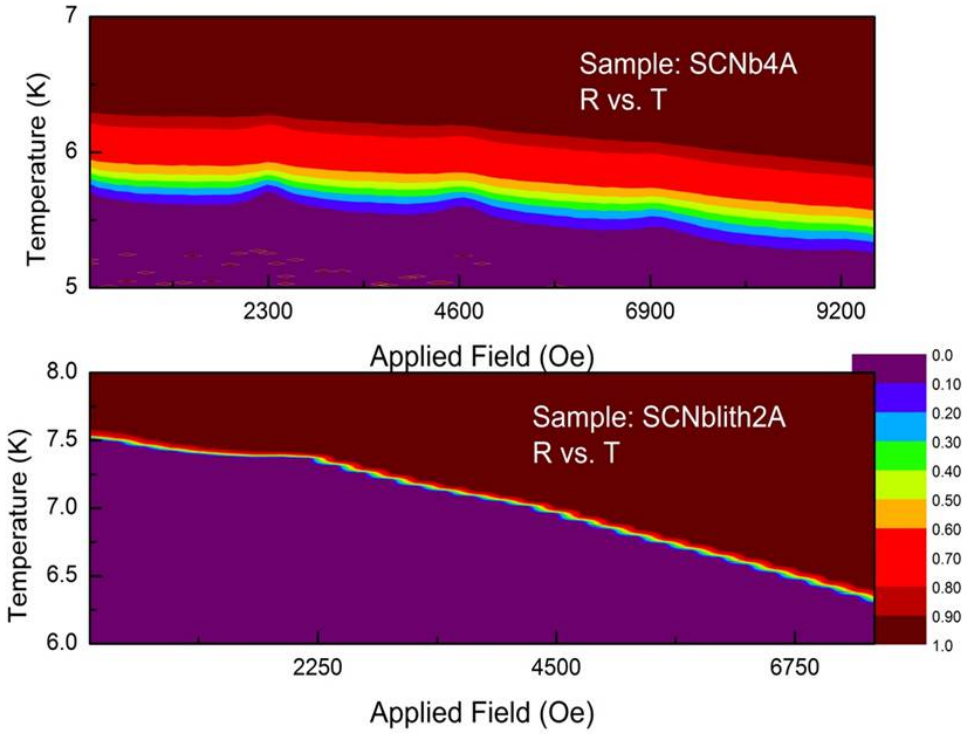

Figure 4.4: Contour plot of samples with different ξ

Color scheme represents the normalized resistance R/R_{Normal} where 1.0 is the normal state. Figure helps illustrate why V vs. B measurements cannot be conducted on samples with a sharp transition temperature (such as SCNblith2A). If a horizontal line is drawn across the above graphs at a fixed temperature, we see that sample SCNb4A has a large field range where it is in a mixed state. Whereas sample SCNblith2A has a very narrow field region in a mixed state. We see that understanding a sample's T vs. B response is important for measurements.

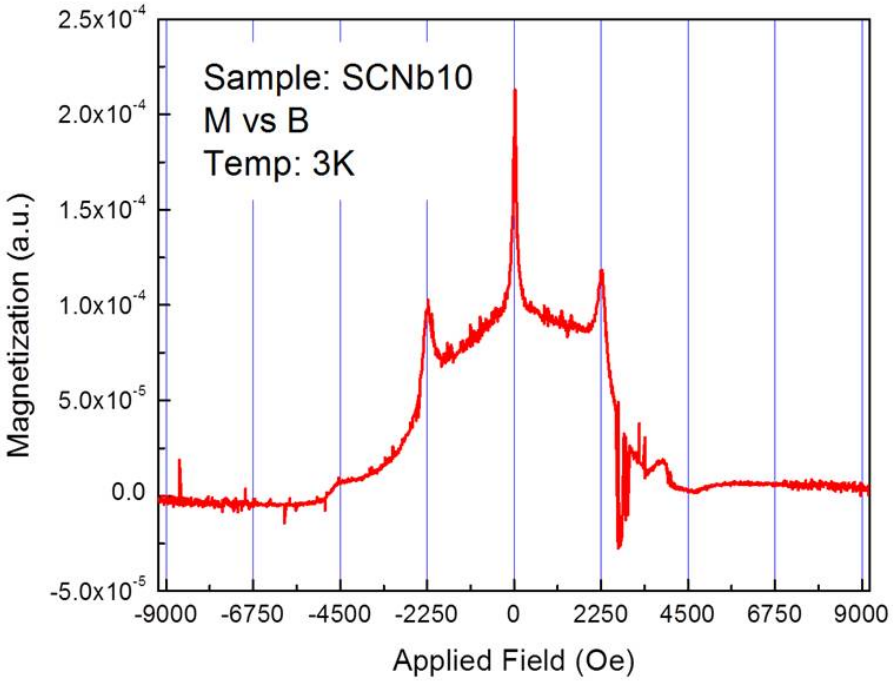

Figure 4.5: Diamagnetic response of sample

Peaks at the matching field (2250 Oe) correspond to a vortex density commensurate with the artificial pinning lattice density and result in a pinned vortex lattice, minimally affecting the superconducting sample and resulting in a large diamagnetic response at the matching field.

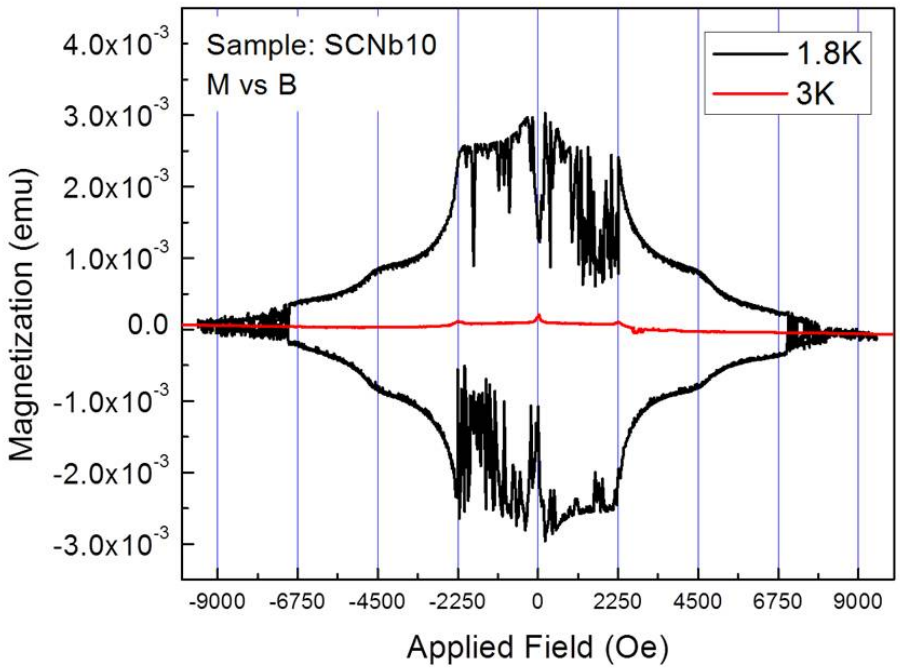

Figure 4.6: Diamagnetic response of sample varying temperature

At a temperature of 1.8 K we can resolve at least three matching effect peaks corresponding to commensurate and interstitial vortex pinning. Scatter in the magnetization data is due to the SQUID loosing sample position during the measurement.

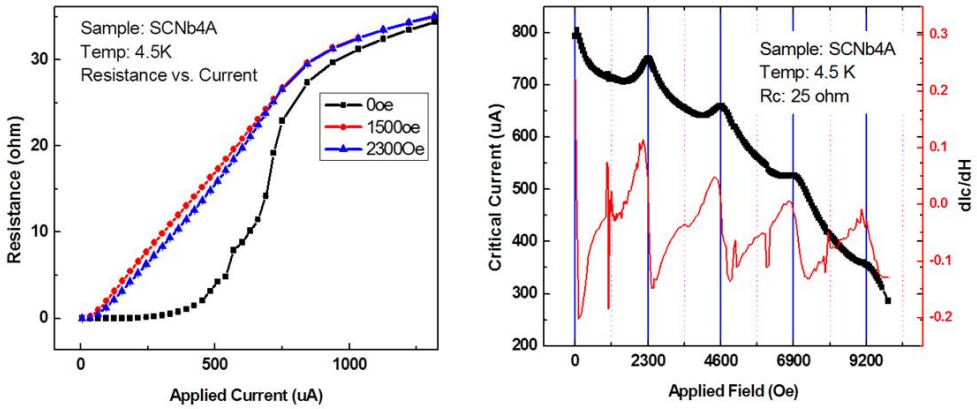

Figure 4.7: Critical current measurements

Plot of resistance vs. applied current (A) and critical current vs. applied field for a threshold resistance of 25 ohms. Figure A shows how the vortex density (field strength) alters the shape of the R vs. I curve. Note at the matching field of 2300 Oe, a lower sample resistance is found compared to the 1500 Oe run. This is indicative of vortex pinning. Figure B is a plot assembled from R vs I plots at different applied fields. Critical current maxima at the matching fields illustrate the flux pinning nature of the anti-dot lattice. The curve in red is a point-by-point derivative of the I_c vs H plot, it clearly shows four maxima at the matching fields, and possibly an additional matching peak at $0.5H_1$.

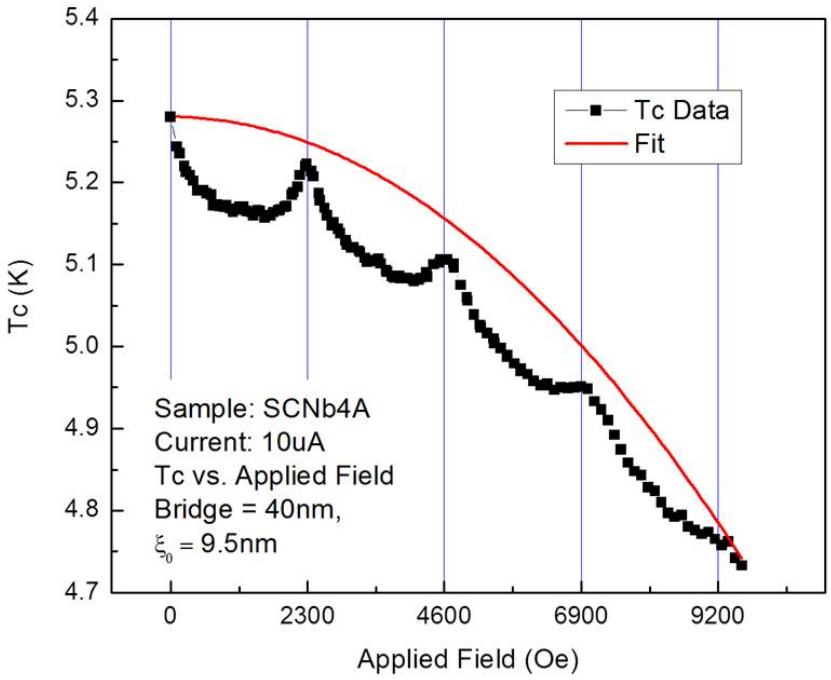

Figure 4.8: T_c vs. Field

Variation of T_c vs applied field using a 25Ω resistance threshold. Peaks at the matching field correspond to Little-Parks oscillations. Matching fields correspond to phase differences of 2π across a pinning site. Red fit line corresponds to a best fit of the $T_c(H)$ peaks using a bridge width of 40 nm and a coherence length of ~ 9 nm.

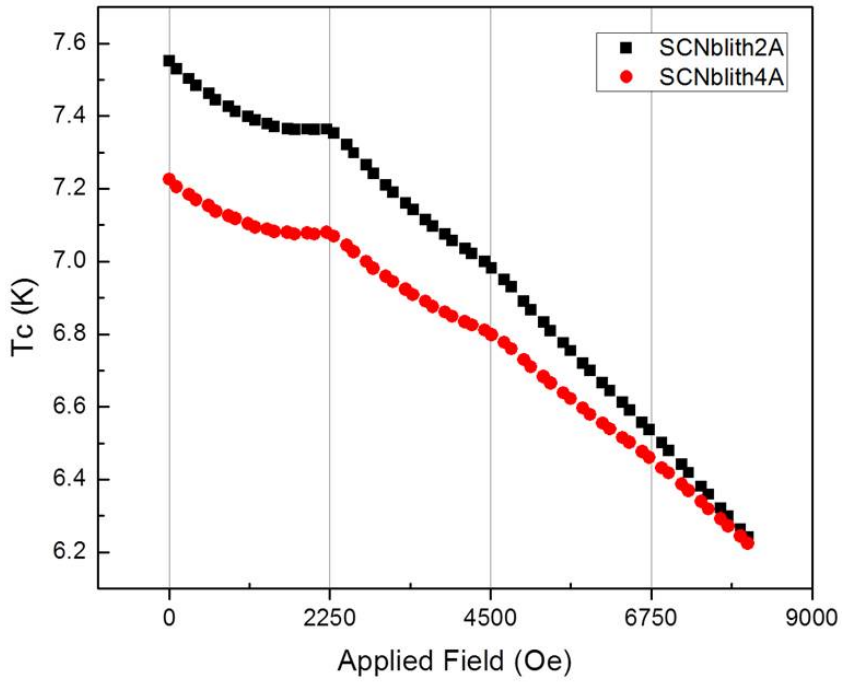

Figure 4.9: T_c vs. Field for different samples

Variation of T_c vs. applied field for sample with coherence length ~ 18 nm. Peaks in T_c are observed for several matching fields, plotting R vs. T results in a better representation of the samples vortex pinning behavior compared with magnetoresistance measurements shown in Fig 4.2.

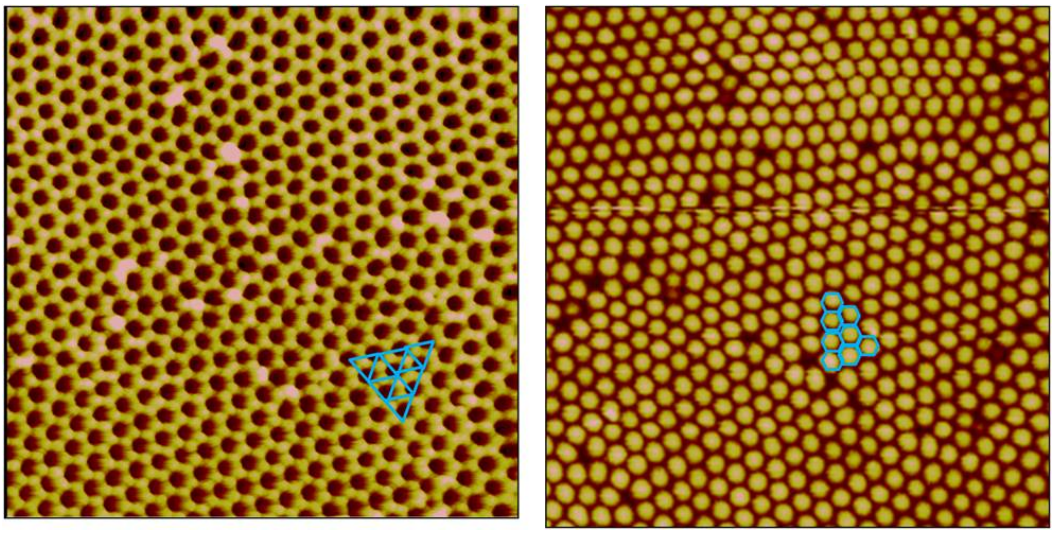

Figure 4.10: AFM scans of triangular (anti-dot) and hexagonal (dot) lattices

$2\mu m^2$ AFM scans of both sides of the alumina templates showing the triangular anti-dot lattice (left) which is the surface used on nearly all measurements. Also shown is the hexagonal dot lattice where vortices should sit in the vertices of the hexagonal lattice. Since the hexagonal lattice is composed of two triangular lattices of $\sim$ 100nm $H_{1Hex} = 2H_{1Triangle}$. The Hexagonal lattice provides an opportunity to change the lattice orientation of our samples.

Chapter 5

Vortex Noise in Nb Films on a Triangular Anti-dot Lattice:

Understanding vortex motion in superconducting materials is a complicated but necessary task in order to maximize a samples current density in the superconducting state. As a current flows in a superconducting film with vortices, a Lorentz force acts on the vortices which can cause them to move. This vortex motion changes the magnetic flux which causes a dissipative voltage that is detected as a resistance ultimately limiting the current density in the superconductor. In a film with pinning sites it may not be surprising this vortex motion would manifest itself as a fluctuating voltage signal, in the 1960's Van Gurp linked these fluctuations to vortices jumping to neighboring pinning sites [33]. While early experiments assumed a vortex flux proportional to the applied current, it has been shown that random pinning sites within a superconducting sample give rise to stochastic voltage peaks due to different vortex depinning thresholds [29, 34]. Further, vortex avalanches have been observed and characterized by their power spectra density (PSD) and suggest self-organized criticality [35, 36]. All of the noise experiments are due to superconducting vortices interacting with some form of pinning site which can vary in size, strength and density; thus observing how vortices interact with well defined periodic pinning sites should shed light onto the motion of vortices.

Resistance and transition temperature (T_c) measurements on superconducting Nb films show a periodic field dependence due to the underlying alumina template with

sub-micron pores arranged in a triangular array. The sample resistance show periodic minima when superconducting vortices become pinned by the normal vacancies in the underlying alumina lattice. The periodic pinning sites change the mobility of the vortices depending upon the vortex density; this is particularly pronounced when the vortex density is commensurate with the artificial pinning sites. Our measurements have focused on the voltage noise generated as vortices are depinned from the artificial lattice. We report the findings of two measurements conducted on our Nb films. Preliminary measurements of the samples voltage noise PSD at a fixed temperature, with a small coherence length ($\xi \sim 10nm$) show periodic field dependence. However, we find that this result masks the influence of T_c. Using samples with a longer coherence length ($\xi \sim 18nm$) and scaling the measurement temperature with the field dependent T_c, we find that our noise measurements are insensitive to the applied field. These measurements illustrate the care that must be taken to avoid attributing field dependent noise to the variation of the transition temperature at the matching fields.

The motion of vortices in a regular pinning array has been modeled extensively using molecular dynamic simulations. The high degree of symmetry in a periodic array of pinning sites allows numerical simulations to be conducted which show the dynamics of different vortex densities in a manageable number of pinning sites. While there are slight variations in the numerical simulation models employed, our analysis follows the dynamics modeled by Charles and Cynthia Reichhardts at the Center of Nonlinear Studies at Los Alamos [32, 21, 18, 20, 37].

Although molecular dynamics simulations consider a small sample volume with perfect pinning site size, lattice spacing and crystal like perfection there is still considerable agreement between experiment and simulation [4, 38]. Thus, simulations of various pinning site/vortex arrangements have proven to be useful references to testing different sample pinning geometries and interpretation of mass vortex motion.

The simulations use a finite sized sample space, typically with periodic boundary conditions. The influence of pinning sites are defined by $\mathbf{f}_i^{vp}$ and a master equation is used to determine the velocity $\mathbf{v}_i$ of a vortex as it interacts with the pinning sites and other vortices $\mathbf{f}^{vv}$ as the driving force $\mathbf{f}_d$ is changed. A more complete description of the terms is given in appendix A.

The ability to track an individual vortex and monitor the effects that vortex density,

pinning site disorder, size and strength play have led to a better understanding of the vortex dynamics in samples with a periodic array of pinning centers [21, 18, 20, 16, 19]. The simulations are particularly relevant to our experiments looking at vortex noise in a superconducting sample because they can indicate different vortex flow regimes and voltage characteristics which occur amidst numerous vortex signals at various vortex densities under a driving force [32, 18, 14, 15].

While simulations have identified different flow phases for a highly ordered pinning lattice similar flow regimes for a disordered pinning lattice show a dependence upon the strength of the vortex-vortex interaction [16]. Simulation results show that the size of the vortex interaction strength can be probed in measurements of the differential resistance dV/dI and by the magnitude of the noise signal generated as a function of the driving current. We will show that our samples, which have a well ordered periodic structure at the length scale of around a micron, possess matching field effects indicative of a well ordered pinning lattice. In general we will show how the simulation results for a disordered lattice compare with the measurements of vortex dynamics in our samples.

Simulations on disordered arrays consider randomly placed columnar defects in a two-dimensional plane. The applied field is held fixed and corresponds to a constant vortex density in the simulation. The vortex-vortex force ($\mathbf{f}^{vv}$) is modified by multiplying by a numerical pre-factor called the vortex interaction strength A_v.

$$\mathbf{f}_i^{vv} = \sum_{j=1}^{N_v} A_v f_0 K_1 \left(\frac{|r_i - r_j|}{\lambda} \right) \hat{\mathbf{r}}_{ij} \tag{5.1}$$

In the limiting cases, if $A_v = 0$, the $\mathbf{f}^{vv} = 0$, vortices are insensitive to each other, and depinning occurs when the driving force is greater than the pinning force ($f_d > f_{v.p.}$) causing a large change in a plot of dV/dI vs. I, at that driving current. When the interaction strength is larger than zero ($A_v > 0$), the depinning force is lowered due to vortex-vortex interactions assisting the vortex depinning i.e. ($f_d + f_{v.v} > f_{v.p.}$). Due to the random placement of the pinning sites, vortex depinning is no longer instantaneous causing a smaller dV/dI response over the range of driving currents as shown in figure 5.1.

The simulations show that the corresponding voltage noise V_f is related to the interaction strength in a non-monotonic fashion. V_f noise occurs when the driving force

($f_d + f_{v.v.} > f_{v.p.}$) such that vortices are displaced from the pinning sites. The noise signal arises from the flow of vortices in the film as they are first depinned and begin hop to adjacent pinning sites until f_d is large enough to cause the vortices to flow across the sample in an ohmic response. Measurements of the peak noise magnitude at a fixed frequency show that the largest noise signal occurs at an intermediate A_v value. We are fortunate to find that A_v is related to the vortex density[16], this is ideal for our experiments because we can easily adjust interaction strength by changing the applied field. (figure 5.1).

Convientently, simulations also show that the maximum noise signal occurs when the vortex flow dynamics change from uncorrelated (individual vortex hopping between nearest neighbor pinning sites without interacting with nearest vortices) to correlated vortex flow (all vortices flow as an organized lattice). This change in flow is associated with an organization of the vortices into an ordered lattice. While the original paper considered vortex motion and depinning due to a random orientation of pinning sites with a vortex to pinning site ratio of $\sim 2/3$ similar results are found in simulations of periodic arrays of pinning sites as well [18, 20, 37, 14, 15].

We compare our measurements to the above simulations, the noise is measured at a fixed frequency below 5 kHz (well within the $1/f$ regime of our noise) using a standard four-terminal IV measurement utilizing a lock-in amplifier and biasing the sample with a DC current. We also measured the current/voltage characteristics of our sample, which allow us to track the superconducting transition of our sample at a fixed magnetic field. The experiment examines how the peak noise varies in each of our samples at various applied fields. Further, it allows a direct comparison to the theory developed in the simulations which provides a straightforward means to identify and classify a change in the vortex dynamics.

A change in vortex dynamics is particularly significant for our samples deposited on a periodic pinning lattice. The vortex lattice can be probed at three separate cases: $H < H_1$, $H > H_1$ and $H = H_1$ simulations suggest a different vortex/pinning site interaction at each case[37]. For applied fields less than H_1 there are empty pinning sites which should favors uncorrelated vortex flow as vortices hop to adjacent empty sites. A similar result is expected for fields greater than H_1 where now interstitial vortices are pinned less strongly and flow between pinned vortices. However, when

$H = H_1$ there are no open pinning sites and no interstitial vortices, which means that all vortices should depin and flow together since there are no vacant spots for the vortices to flow to. This large scale collective motion tells us that if our periodic pinning lattice affects the vortex noise in our system.

At this point we should indicate that we have no predicted spectral behavior for the transition from correlated to uncorrelated vortex motion. We only expect a comparative increase in peak noise amplitude as uncorrelated vortex motion becomes correlated. This suggests that we will measure a lower noise amplitude below H_1 where vortex motion should be uncorrelated, and a similar signal when weakly pinned interstitial vortices are added above H_1. At H_1 we expect the vortex motion to be correlated and we should detect the largest peak in noise if we measure at a fixed frequency.

5.1 Constant Temperature Noise Measurements

Unless otherwise specified, the PSD of our vortex noise was measured using a HP-35670A Spectrum Analyzer. While a measurement of a sample's power spectra is easy to conduct, detecting a noise signal in a superconducting sample is difficult as even the background Johnson noise ($S_v = 4k_bTR$) of a superconducting sample at a resistance $R = 0$, and temperature $T < 10$ K is well below our detector background signal $\sim 10^{-15}V^2/Hz$. Thus as we explore the large superconducting phase space, we spend a good deal of time looking for changes in the background signal. As a way to quickly examine hundreds of power spectra we find that plotting the spectra as an intensity plot allows us to quickly observe where there are changes in vortex noise and how that signal evolves as the current or field is varied. A representative noise intensity plot is shown in figure 5.2 as well as a power spectra slice at -1550 Oe (inset) showing how the colors of the intensity plot relate to the noise power spectrum.

We have conducted several noise measurements looking at the voltage noise as a function of either applied field at a fixed current or applied current at a fixed field using a lock-in amplifier at a fixed frequency, or a spectrum analyzer to measure the noise as a function of field or bias current. In all measurements the voltage noise signal corresponds to voltage fluctuations from mobile vortices at the measured frequency. We find that the noise signal depends upon the sample temperature, bias current and

applied field. Our initial noise measurements were conducted on samples with broad superconducting transitions and a small coherence length ($\sim$ 10 nm). These samples show field dependence in the noise power spectra that oscillate in noise magnitude at the matching field of $\sim 2250 - 2300$ Oe (see figures 5.4 and 5.3). Measurements of noise vs. driving current at specific vortex densities show a phase diagram where the size of the spectra change depending upon the driving current. While these initial measurements show a significant noise response we had concerns with the Nb film quality (low T_c, small ξ) these issues led to broad superconducting transitions and meant the vortex density $n_s > 1$ indicating multiple vortex pinning at a pinning site was possible.

We made several improvements to the film deposition process, referenced in chapter 4. These improvements led to an increase in the ξ and produced a sharper superconducting transition edge. We can observe the change in the superconducting transition by examining the figure 4.4 which illustrates the dramatic improvement in superconducting transition width in a Temperature vs. Field intensity plot.

Our initial vortex noise measurements were conducted on 100 nm thick Nb films deposited upon alumina templates through a shadow mask. They were large samples with a $T_c \leq 6K$ and a large transition region of $\sim$ 1 K. While the Nb film quality was not ideal, the vortex noise of the sample was very interesting. The power spectra measured across $2 - 3$ matching fields at a fixed current (between $0.6 - 2$ mA) and a constant temperature of 4.2 kelvin displayed a $1/f - 1/f^2$ power spectra that varied with applied field as shown in figures 5.4 and 5.3. Here white regions are a high noise region and the dark blue corresponds to the noise floor of the spectrum analyzer. Both show that a field and current dependent response in the voltage noise. While the noise signal is intriguing, measurements of R vs. T as a function of field show that the transition temperature T_c varies with the applied field, such that T_c maxima are observed at the matching fields (Figure 4.4). This fluctuation of T_c changes the pinning strength of the lattice, suppressing vortex motion and noise. Therefore, we must decouple our noise measurements from any temperature dependent effects; probing only the response from the vortex/pinning site ratio. This is done by tracking the temperature such that the sample resistance is 15% of the normal resistance at a fixed excitation current of 1 mA. Using this resistance threshold we hope isolate the noise signal due to the artificial pinning lattice and not an effect related to enhanced T_c at the matching field(s).

5.2 Temperature Independant Noise Measurements

With the refinements to our deposition process mentioned in chapter 3 we increased our $T_c > 7K$ with a coherence length of ~ 18 nm, which is still in the dirty limit, but comparable to other measurements using Nb. Measurements of the matching field, $\xi(0)$ and reduced temperature T/T_c are made by conducting a Little-Parks type experiment and are described in detail in chapter 4. Here T/T_c is defined as the temperature at which a DC current bias of $0.6mA$ produces a 1Ω response across the film at a given field. This 1Ω measurement temperature criterion was used at each field value and resulted in a nearly identical depinning/peak noise current (I_c) across the field range we investigated. At this T/T_c we also measure a relatively smooth transition from the superconducting to normal state. Inset of figure 5.5 shows a plot of R vs. T as the applied field is increased, the horizontal line indicates the resistance threshold used to define T/T_c at a specific field. This data is then used to plot T/T_c vs. H. Matching effects occur at a field multiples of (2250 Oe) which is in good agreement with our 100 nm anti-dot triangular lattice. We include data from a witness film which shows no periodic field effects, only a linear decrease in T/T_c as the field is increased.

While many samples were deposited using a shadow mask, there is a question about sample thickness at the edges of these samples. Therefore, we conducted noise measurements on anti-dot templates that have lithographically defined boundaries. While defining the boundaries was challenging due to the fragile nature of the alumina templates, we fabricated several samples that repeatably displayed a sharp and narrow T_c transition, a relatively high $T_c > 7.2K$ and matching fields of 2250 Oe.

Vortex noise measurements on the lithographic samples was conducted at a fixed field and temperature, a DC current bias is slowly increased and vortex noise is measured by either a Spectrum analyzer or a lock-in amplifier at a fixed frequency. A representative noise data at a fixed frequency, along with the voltage and peak noise at different fields on a witness film are shown in figure 5.6. In general the noise spectra show a power spectrum that is roughly $1/f$ at the bias current where the vortices depin.

Our measurements of the sample noise at a constant frequency, field and reduced temperature, show that the noise peak occurs at roughly the same bias current, which indicates that we are measuring the vortex depinning only, removing the influence of

temperature. We measure the vortex noise across a field range spanning 800-5000 Oe (from below H_1 to above H_2) and follow the analysis performed in simulations (Figure **??**). We plot the peak noise signal at each field versus applied field. Simulations[37] suggest that the vortex noise should result from different flow regimes as the vortices are depinned and that the flow phases will change below, above and at the matching fields.

While simulations suggest different flow phases and a change in vortex noise at different vortex densities, we find no such evidence in our vortex noise measurements. Examining a representative plot (figure 5.7) of the voltage and vortex noise at constant frequency vs. DC Bias current shows that the voltage evolves from a superconducting sample then transitions normal at which point the voltage shows a linear (ohmic) response. Meanwhile the noise response starts at a very small value and evolves to a maximum an order of magnitude larger than the initial signal. We expect the shape of the noise vs. DC bias to be similar at every applied field since each curve represents the response of vortices depinning. However, the peak noise amplitude at each field should change as the vortex flow changes from uncorrelated to correlated motion as the vortex density is increased. As we might expect, the peak noise occurs at the point of largest voltage change between the superconducting to normal state. At this point, we expect a large fraction of vortices are mobile, as the sample transitions normal, vortices are destroyed and the noise level falls to the background level. We note that this response is independent of DC bias sweep direction, showing no hysteresis in the voltage or vortex noise signals.

We plot the peak noise signal from multiple samples, over numerous runs, spanning several matching fields; we find that the data shows no correlation with the matching field. (figure 5.8 and 5.9). This indicates a similar vortex flow above below and at the matching field, and that unlike previous simulations [37, 15], the vortex dynamics does not change at H_1 or when interstitial vortices are added.

5.3 Discussion

Our results imply that there is no change from uncorrelated to correlated vortex motion as a function of vortex density. The fact that there is essentially a constant noise

response indicates that the vortex flow is always correlated or uncorrelated. If we first consider the case where the vortex flow is always correlated, the result wouldn't be a surprise if we were looking at the field region containing H_1 and above. Here, the pinning lattice is filled and has to absorb the stress from any interstitial vortices. But it seems hard to believe that we should have the same correlated vortex motion at fields $\sim 0.5H_1$ where open pinning sites exist.

If the vortex flow was always uncorrelated there should be a mechanism for allowing some of the vortices to flow. One such mechanism could be the incomplete lattice order in our templates at the edges of our ordered triangular crystallites. While we observe the triangular order existing in crystallites roughly a square micron in size, our samples are roughly a mm^2 in size. Therefore, we should consider what fraction of our sample consists of crystal boundaries. A rough estimate can be made by considering that a $1\mu m^2$ crystallite has around 100 ordered anti-dots each separated by 100 nm. We can solve for the four sides of a $1\mu m^2$ of pinning sites in a square lattice ($4 \times 1\mu m/100nm = 40$) and find that in each ordered crystallite there will be 100 ordered anti-dots surrounded by roughly 40 anti-dots at a the boundary. This implies that up to 40% of our pinning sites consist of pinning site boundaries, it is possible that these sites could form wider/irregular dispersive channels where vortex motion is preferred [37]. If this is the case our peak noise signal is due to a vortex avalanche as they are depinned from the ordered anti-dots, but riding on top of a very small background signal from weakly pinned vortices in the channels [31, 28]. Naturally we expect this effect to be more pronounced as we change the driving current, which effectively samples the pinning strength of all pinning sites.

However, even with a large fraction of lattice defects, we still see multiple matching effects in R, T_c and I_c measurements versus field. This implies that the ordering of the vortex lattice is still quite strong. The robust nature of the pinning effects also implies a significant amount of correlation/interaction in the vortex lattice.

We therefore expect that the nearly uniform noise response across all measured fields (figures 5.8, 5.9) is most likely due to highly correlated vortices. This behavior is also indicative of a strong vortex-vortex interaction[16].

Highly correlated vortex motion would be expected if the vortices interact strongly

with each other. We can make an estimate of this vortex interaction strength by comparing the mean vortex spacing to the perpendicular penetration depth of the vortices which is given by the Pearl length[39] ($\Lambda = 2\lambda^2/d$). Where λ is the penetration depth and d is the sample thickness. If we use the typical values for our Nb of $t = 100nm$ and a $\lambda \simeq 100nm$ we find $\Lambda \approx 200nm$. This tells us that we should expect strong vortex-vortex interactions and correlated vortex motion as long as our average vortex spacing is $>$ 200 nm or 500 Oe for our samples, which is a significantly lower field than H_1.

Our results show that the vortex noise we measured is due to correlated vortex motion in our periodic pinning samples. It is surprising that the vortex-vortex interaction, not the 100 nm anti-dot lattice is the force that is responsible for correlated vortex motion. Still the results serve as a guide suggesting new pinning templates with similar diameter pores but a lattice spacing $\geq \Lambda$. At this revised length scale, the penetration depth becomes comparable to the lattice spacing, and the vortex dynamics should be dominated by the periodic lattice. These possibilities provide many possibilities to further understand vortex noise.

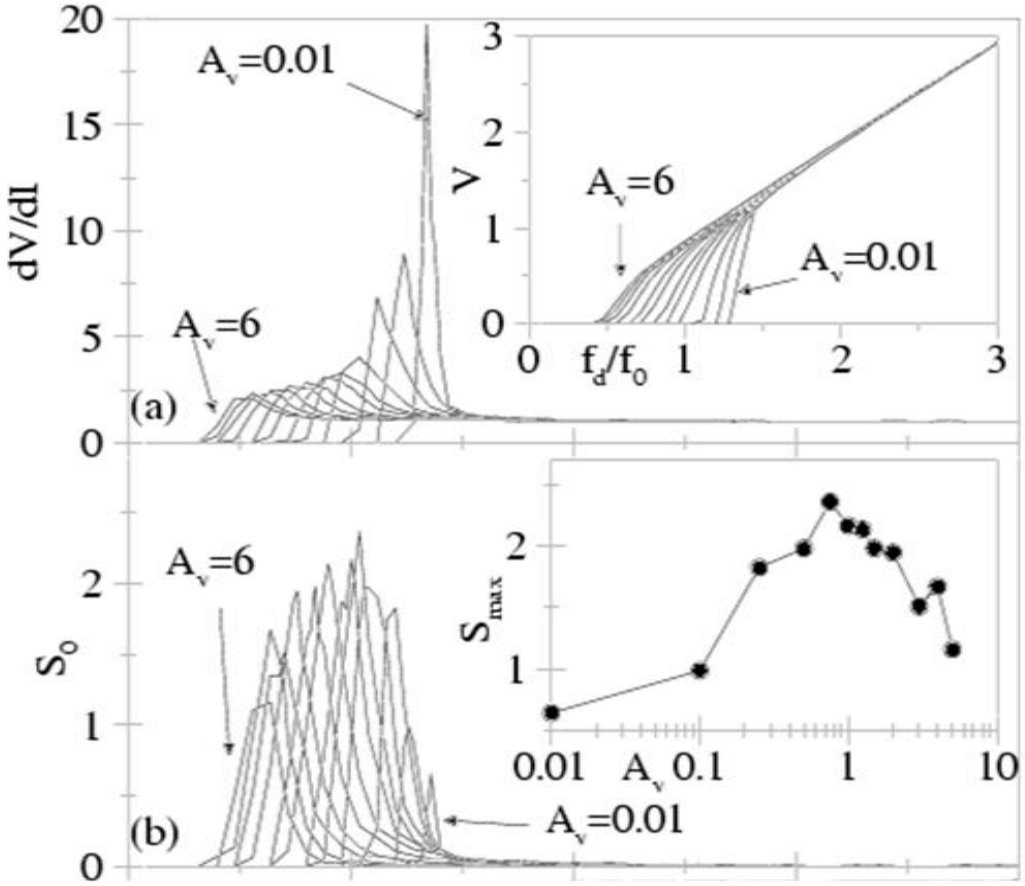

Figure 5.1: Simulations varying the vortex interaction strength A_v

Plots of differential resistance (top) show that as vortex interaction strength decreases the resistance peak increases. Noise peak versus driving force (bottom) show that the noise signal depends upon the vortex interaction strength A_v. Bottom inset shows the how the peak noise signal is a non-monotonic function of A_v, the largest noise signal occurs when there is a change in vortex motion from a uncorrelated to correlated vortex motion [16].

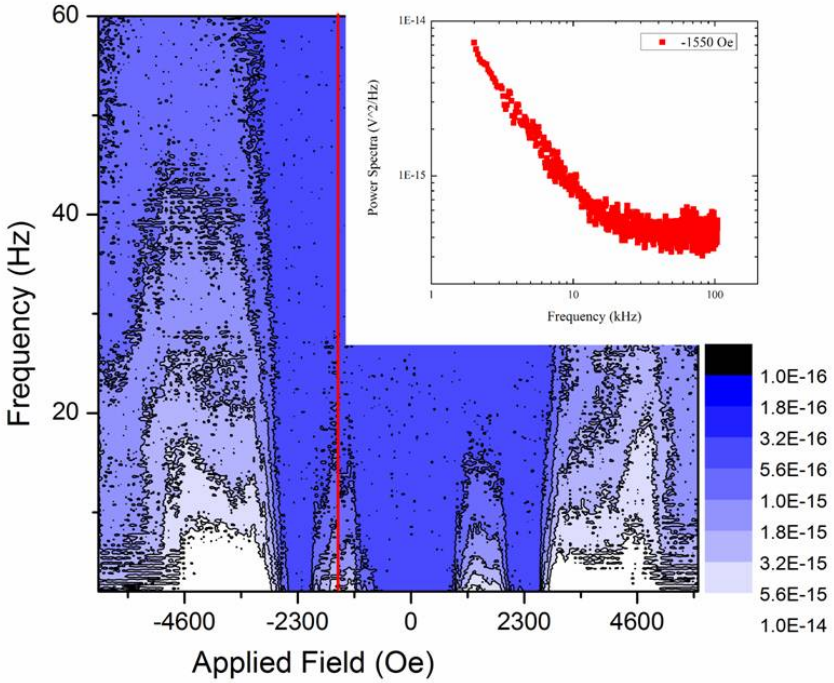

Figure 5.2: Representative Noise Intensity plot.

Intensity plots provide a way to observe changes in vortex noise as a parameter, such as magnetic field, is changed. The intensity plot is assembled from numerous power spectra with each color representing a noise threshold level. The vertical red line at -1550 Oe is a slice of the intensity plot the corresponding vortex noise power spectrum is shown in the inset.

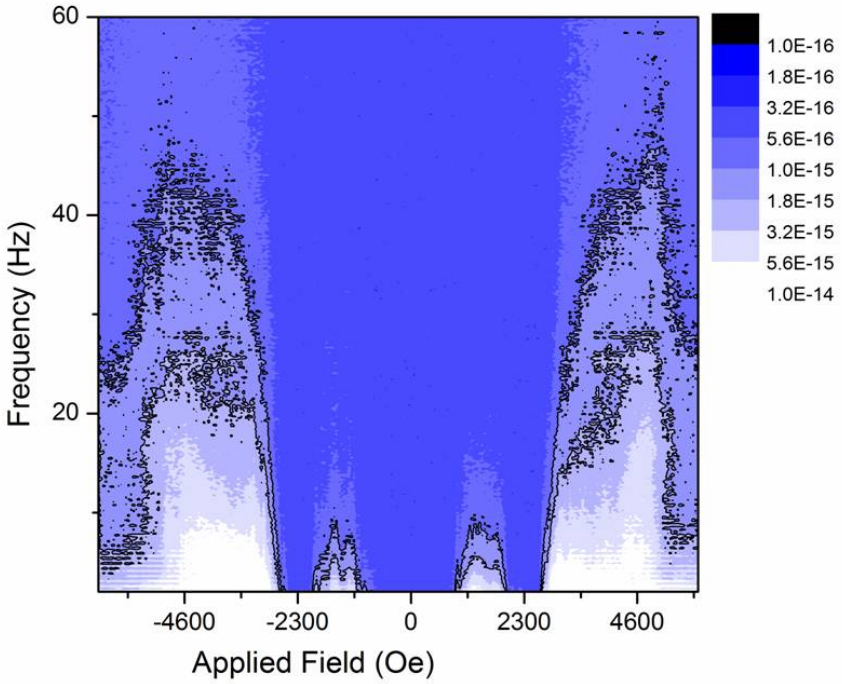

Figure 5.3: Vortex Noise vs. Field Intensity Plot

Contour plot of noise spectra vs. applied field sample SCNb4A at a constant DC bias current of 2.1 mA. Dark line illustrates the contour of 1E-15 V^2/Hz and shows how the noise signal is attenuated at the samples first matching field (2375 Oe).

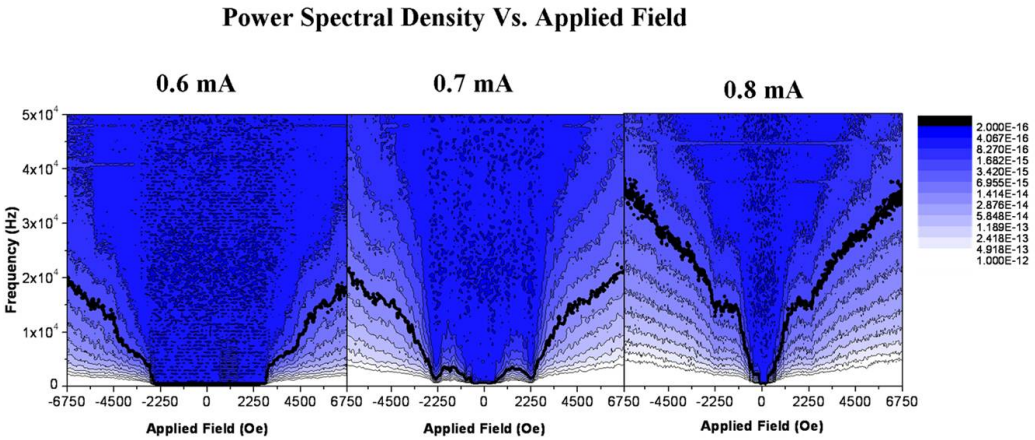

Figure 5.4: Vortex Noise Intensity Plot, Varying Bias Current.

Contour plots showing the field dependence of sample BCNb6 as the field is swept. Threee different plots show how the noise response changes at different bias currents, dark black line serves as a constant threshold in all the figures. We see that the noise signal remains a local minima at the samples first matching field.

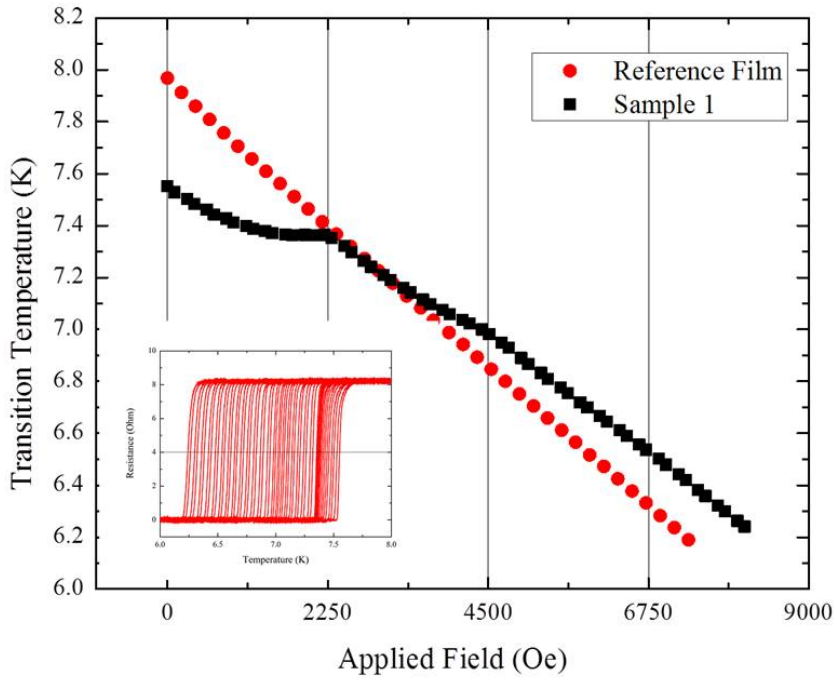

Figure 5.5: T_c vs. H plot

T_c vs. Applied field for sample showing an increase in $T_c(H)$ at the matching field(s). Inset shows R vs. T plots at various applied fields showing the variation in T_c as field is increased. Horizontal line at 4Ω represents the field dependent resistance threshold chosen to define T_c.

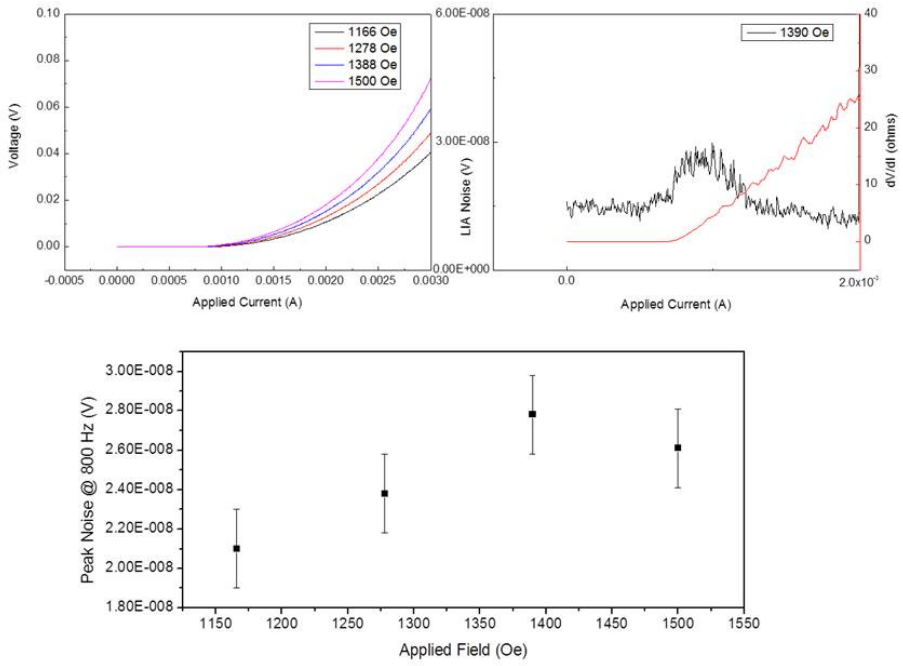

Figure 5.6: Noise measurements on witness film.

Figure shows voltage vs. current, Noise at 800 Hz and differential resistance vs. current and the peak noise vs. applied field for a witness sample. Note, these samples have no artificial pinning lattice.

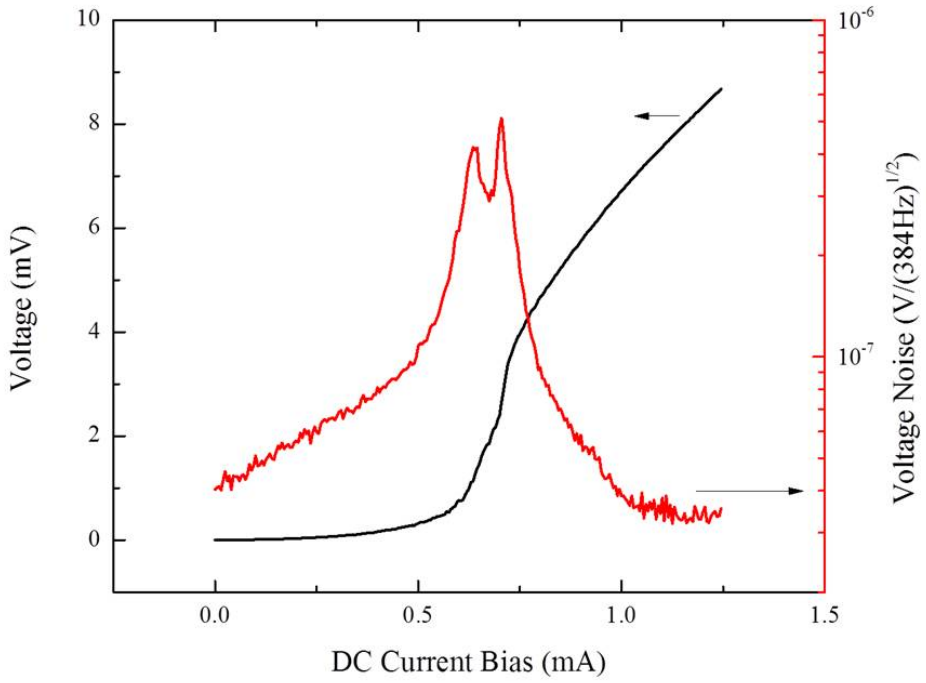

Figure 5.7: Voltage and vortex noise vs. DC Bias Current.

Representative DC Voltage and vortex noise (at 384 Hz) versus DC current bias at a field of 2250 Oe. A noise peak occurs when at a DC current of $\sim 0.7mA$.

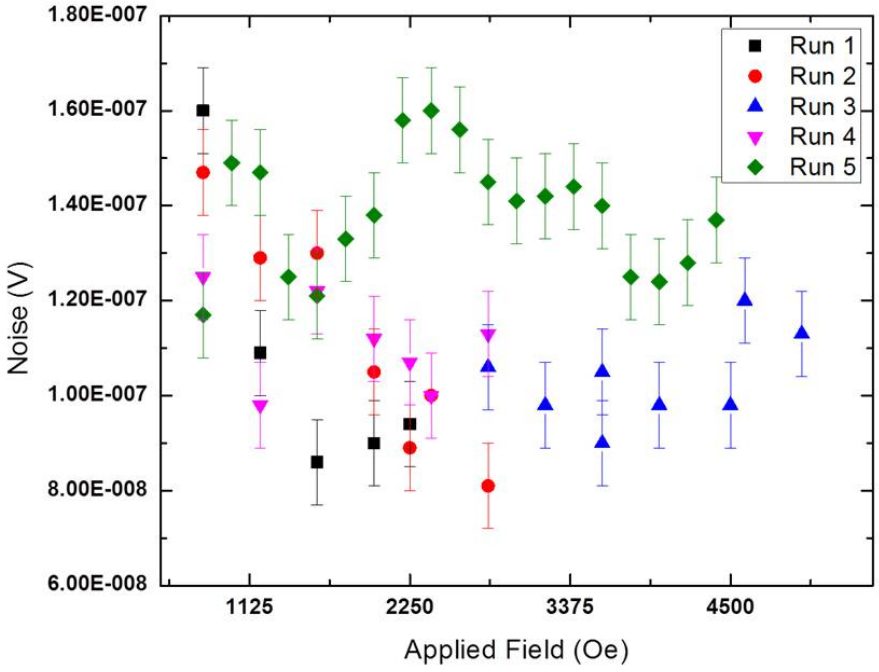

Figure 5.8: Peak noise vs. Field SCNblith2a

Plots of the peak noise signal from voltage vs. DC current bias sweeps at the indicated fields. Here we see no strong correlation with the vortex noise and the matching field.

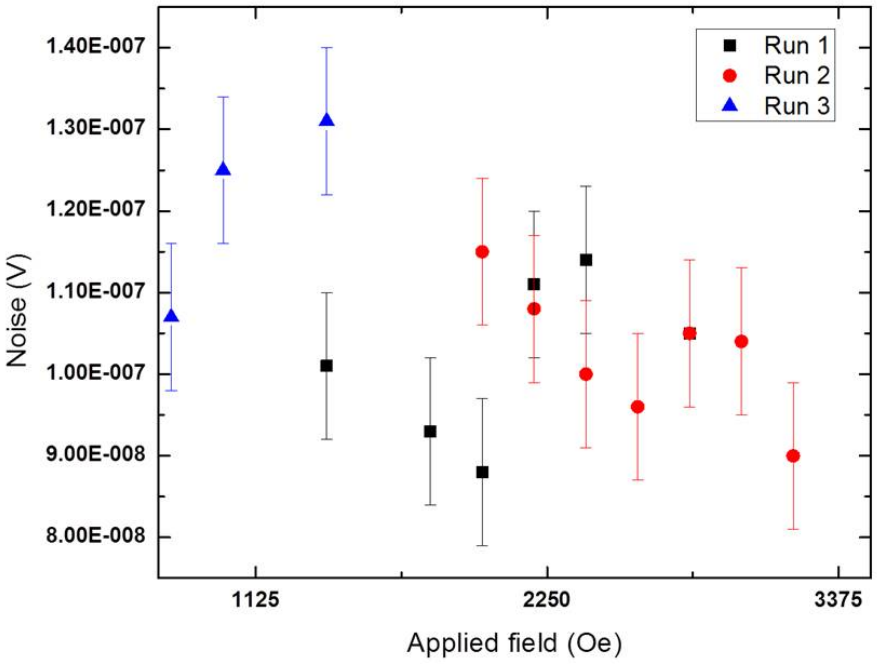

Figure 5.9: Peak noise vs. Field SCNblith4a

Plot of peak noise vs. field. Again we see no correlation of the noise signal to H_1, indicating that the vortex flow remains unchanged as a function of field.

References

[1] Michael Tinkham. *Introduction to superconductivity*. Courier Dover Publications, 2004.

[2] Charles Kittel. *Introduction to Solid State Physics*. Wiley, 8 edition, November 2004.

[3] H. F. Hess, R. B. Robinson, R. C. Dynes, J. M. Valles, and J. V. Waszczak. Scanning-tunneling-microscope observation of the abrikosov flux lattice and the density of states near and inside a fluxoid. *Physical Review Letters*, 62(2):214–216, January 1989.

[4] K. Harada, O. Kamimura, H. Kasai, T. Matsuda, A. Tonomura, and V. V. Moshchalkov. Direct observation of vortex dynamics in superconducting films with regular arrays of defects. *Science*, 274(5290):1167 –1170, November 1996.

[5] A. Hoffmann, P. Prieto, and Ivan K. Schuller. Periodic vortex pinning with magnetic and nonmagnetic dots: The influence of size. *Physical Review B*, 61(10):6958, March 2000.

[6] Y. Jaccard, J. I. Martn, M.-C. Cyrille, M. Velez, J. L. Vicent, and Ivan K. Schuller. Magnetic pinning of the vortex lattice by arrays of submicrometric dots. *Physical Review B*, 58(13):8232, October 1998.

[7] J. I. Martin, M. Velez, J. Nogues, and Ivan K. Schuller. Flux pinning in a superconductor by an array of submicrometer magnetic dots. *Physical Review Letters*, 79(10):1929, 1997.

[8] J. I. Martin, M. Velez, A. Hoffmann, Ivan K. Schuller, and J. L. Vicent. Temperature dependence and mechanisms of vortex pinning by periodic arrays of ni dots in nb films. *Physical Review B*, 62(13):9110, October 2000.

[9] Wai-Kwong Kwok, Z. L. Xiao, U. Welp, A. Rydh, V. Vlasko-Vlasov, and V. Novosad. Commensurate vortex pinning in nb films patterned onto anodized aluminum oxide. *Physica C: Superconductivity*, 412-414(Part 1):347–351, October 2004.

[10] J. Vanacken, W. Vinckx, V.V. Moshchalkov, S. Matefi-Tempfli, M. Matefi-Tempfli, S. Michotte, L. Piraux, and X. Ye. Vortex pinning in superconductors laterally modulated by nanoscale self-assembled arrays. *Physica C: Superconductivity*, 468(7-10):585–588, April 2008.

[11] W. Vinckx, J. Vanacken, V. V. Moshchalkov, S. Matefi-Tempfli, M. Matefi-Tempfli, S. Michotte, and L. Piraux. Vortex pinning in superconducting nb thin films deposited on nanoporous alumina templates. *The European Physical Journal B*, 53(2):199–203, October 2006.

[12] U. Welp, Z. L. Xiao, J. S. Jiang, V. K. Vlasko-Vlasov, S. D. Bader, G. W. Crabtree, J. Liang, H. Chik, and J. M. Xu. Vortex pinning in nb films patterned with nanoscale hole-arrays. *Physica B: Condensed Matter*, 329-333(Part 2):1338–1339, May 2003.

[13] Jia Zou, Xiaoyuan Qi, Liwen Tan, and Bethanie J. H. Stadler. Large-scale ordering of porous si using anodic aluminum oxide grown by directed self-assembly. *Applied Physics Letters*, 89(9):093106, 2006.

[14] C. J. Olson, C. Reichhardt, and Franco Nori. Superconducting vortex avalanches, voltage bursts, and vortex plastic flow: Effect of the microscopic pinning landscape on the macroscopic properties. *Physical Review B*, 56(10):6175, 1997.

[15] C. J. Olson, C. Reichhardt, J. Groth, Stuart B. Field, and Franco Nori. Plastic flow, voltage noise and vortex avalanches in superconductors. *Physica C: Superconductivity*, 290(1-2):89–97, October 1997.

[16] C. J. Olson, C. Reichhardt, and Franco Nori. Nonequilibrium dynamic phase diagram for vortex lattices. *Physical Review Letters*, 81(17):3757, October 1998.

[17] C. Reichhardt, J. Groth, C. J. Olson, Stuart B. Field, and Franco Nori. Spatiotemporal dynamics and plastic flow of vortices in superconductors with periodic arrays of pinning sites. *Physical Review B*, 54(22):16108, December 1996.

[18] C. Reichhardt, C. J. Olson, and Franco Nori. Dynamic phases of vortices in superconductors with periodic pinning. *Physical Review Letters*, 78(13):2648, March 1997.

[19] C. Reichhardt and C. J. Olson Reichhardt. Switching and jamming transistor effect for vortex matter in honeycomb pinning arrays with ac drives. *Physical Review B*, 81(2):024510, January 2010.

[20] C. Reichhardt, G. T. Zimanyi, R. T. Scalettar, A. Hoffmann, and Ivan K. Schuller. Individual and multiple vortex pinning in systems with periodic pinning arrays. *Physical Review B*, 64(5):052503, June 2001.

[21] Charles Reichhardt and Niels Gronbech-Jensen. Critical currents and vortex states at fractional matching fields in superconductors with periodic pinning. *Physical Review B*, 63(5):054510, January 2001.

[22] Warren DeSorbo. Effect of dissolved gases on some superconducting properties of niobium. *Physical Review*, 132(1):107, October 1963.

[23] Mauro M. Doria and Gilney Figueira Zebende. Multiple trapping of vortex lines by a regular array of pinning centers. *Physical Review B*, 66(6):064519, 2002.

[24] M. M. Doria, S. C. B. de Andrade, and Edson Sardella. Maximum number of flux lines inside columnar defects. *Physica C: Superconductivity*, 341-348(Part 2):1199–1200, November 2000.

[25] G. S. Mkrtchyan and V. V. Schmidt. *Sov. Phys. JETP*, 34:195, 1972.

[26] Xavier Hallet, Maria Matifi-Tempfli, Sebastien Michotte, Luc Piraux, Johan Vanacken, Victor V Moshchalkov, and Stefan Matefi-Tempfli. Quasi-hexagonal

vortex-pinning lattice using anodized aluminum oxide nanotemplates. *Small*, 5(21):2413–2416, November 2009.

[27] W. A. Little and R. D. Parks. Observation of quantum periodicity in the transition temperature of a superconducting cylinder. *Physical Review Letters*, 9(1):9, July 1962.

[28] W. J. Yeh and Y. H. Kao. Measurements of flux-flow and 1/f noise in superconductors. *Physical Review Letters*, 53(16):1590, October 1984.

[29] W. J. Yeh and Y. H. Kao. Flux-flow noise in type-II superconductors. *Physical Review B*, 44(1):360, July 1991.

[30] S. Hirano, Y. Hirata, S. Kuriki, M. Matsuda, T. Morooka, and S. Nakayama. Vortex dynamics of nb variable-thickness bridges measured by direct flux detection method. *Journal of Applied Physics*, 85(11):7819, 1999.

[31] Stuart Field, Jeff Witt, Franco Nori, and Xinsheng Ling. Superconducting vortex avalanches. *Physical Review Letters*, 74(7):1206, February 1995.

[32] C. Reichhardt, G. T. Zimanyi, and Niels Gronbech-Jensen. Complex dynamical flow phases and pinning in superconductors with rectangular pinning arrays. *Physical Review B*, 64(1):014501, June 2001.

[33] G. J. Van Gurp. Flux-transport noise in type-II superconductors. *Physical Review*, 166(2):436, February 1968.

[34] J G Park. Flux motion, electrical resistance and noise in superconductors. *Journal of Physics C: Solid State Physics*, 2(4):742–750, April 1969.

[35] Per Bak, Chao Tang, and Kurt Wiesenfeld. Self-organized criticality: An explanation of the 1/f noise. *Physical Review Letters*, 59(4):381, July 1987.

[36] Per Bak, Chao Tang, and Kurt Wiesenfeld. Self-organized criticality. *Physical Review A*, 38(1):364, July 1988.

[37] C. Reichhardt, C. J. Olson, and Franco Nori. Nonequilibrium dynamic phases and plastic flow of driven vortex lattices in superconductors with periodic arrays of pinning sites. *Physical Review B*, 58(10):6534, 1998.

[38] Akira Tonomura. Direct observation of thitherto unobservable quantum phenomena by using electrons. *Proceedings of the National Academy of Sciences of the United States of America*, 102(42):14952 –14959, October 2005.

[39] J. Pearl. CURRENT DISTRIBUTION IN SUPERCONDUCTING FILMS CARRYING QUANTIZED FLUXOIDS. *Applied Physics Letters*, 5(4):65–66, August 1964.

[40] C. Reichhardt, C. J. Olson, and Franco Nori. Commensurate and incommensurate vortex states in superconductors with periodic pinning arrays. *Physical Review B*, 57(13):7937, April 1998.

[41] William E. Boyce and Richard C. DiPrima. *Elementary Differential Equations*. Wiley, 9 edition, October 2008.

[42] T. Schulz, G. Burch, A. Kunz, and E. D Dahlberg. Magnetic response versus lift height of thin ferromagnetic films. *Magnetics, IEEE Transactions on*, 46(6):1752–1754, June 2010.

[43] J. Lohau, S. Kirsch, A. Carl, G. Dumpich, and E. F Wassermann. Quantitative determination of effective dipole and monopole moments of magnetic force microscopy tips. *Journal of Applied Physics*, 86(6):3410–3417, September 1999.

Appendix A

Vortex Simulations

By employing imaging/detection techniques such as Lorentz Microscopy[4] or a pick-up coil[31] there exists a possibility to directly track various arrangements of superconducting vortices in a sample. However, making sense of such vortex data requires an understanding of how the vortices interact with each other. To date there have been many vortex dynamic simulations conducted on test cases ranging from a high degree of pinning site symmetry, to a random collection of pinning sites [14, 15, 20, 40]. In this way, these simulations become applicable to both our samples with periodic arrays of pinning sites, as well as superconducting films with intrinsic pinning sites. The simulations provide the possibility to track the trajectories of individual vortices as they traverse the sample and interact with pinned and mobile vortices. The velocity of each individual vortex is proportional to the voltage it would generate by Lenz's law. Thus, by monitoring the velocity of the simulated vortices it is possible to understand possible vortex flows, as well as the type of voltage noise that would result as the vortices are driven in the sample [15, 16, 17, 32, 19].

In my time waiting for samples to cool, I developed this vortex simulation in LabVIEW. I sought to replicate previous simulations and hopefully better understand the vortex/pinning site interactions on our Nb films. Since our samples are made on an insulating alumina template with a triangular anti-dot lattice, the pinning site geometry lends itself to simulation without too much difficulty.

If we consider our alumina anti-dot template, it has a lattice spacing of ~ 100 nm with ordered crystallites extending approximately 1 μm, for our samples approximately

1 mm^2 in size. In my time working with the simulation, I attempted to model a single ordered crystallite with a specified driving force (current) direction. To make the simulation more realistic, additional crystallites at different lattice orientations could be represented by changing the current direction and summing the x and y components of each pinning space. In this way, the simulation would attempt to granulize the pinning array and try to understand how the velocity of the vortices in each ordered crystallite adds to produce a net signal across a sample.

A.1 Simulation Details

The simulation was programmed in National Instruments LabVIEW 8.2. However, no claim is made that it is the best programming language for this task, the extensive tracking of individual vortices lends itself to MATLAB, or C++. LabVIEW was chosen due to existing experience, availability and the relative ease of incorporating a graphical display and power spectra measurements. As the simulations were conducted, it became apparent that a different programming language may result in quicker calculations, particularly for large vortex/pinning site densities. Such improvements are left to the reader, with the hope that this appendix serves as a guide illustrating the conditions and measurements I used in my simulations.

While the visual front end of the program was not necessary, it provided a means to observe the pinning sites and vortices in my simulations see figure A.1. Furthermore, it served as simple means for checking the dynamics of the vortices e.g. vortices repelled each other, empty pinning sites would capture a vortex and the periodic boundary conditions were properly implemented. The simulation was conducted by implementing the over-damped equation employed by Charles and Cynthia Reichhardt [40, 15]. These simulation results are also used to check the function of the simulation.

As mentioned in chapter 5, an over-damped master equation is employed to calculate the velocity of a vortex by summing the forces on an individual vortex from its nearest neighbors, any pinning potential and the driving current the vortex feels.

$$\mathbf{f}_i = \mathbf{f}_i^{vv} + \mathbf{f}_i^{vp} + \mathbf{f}_d = \eta \mathbf{v}_i \tag{A.1}$$

Where $\mathbf{f}_i$ is the total force felt on a vortex at i, which is composed of forces from

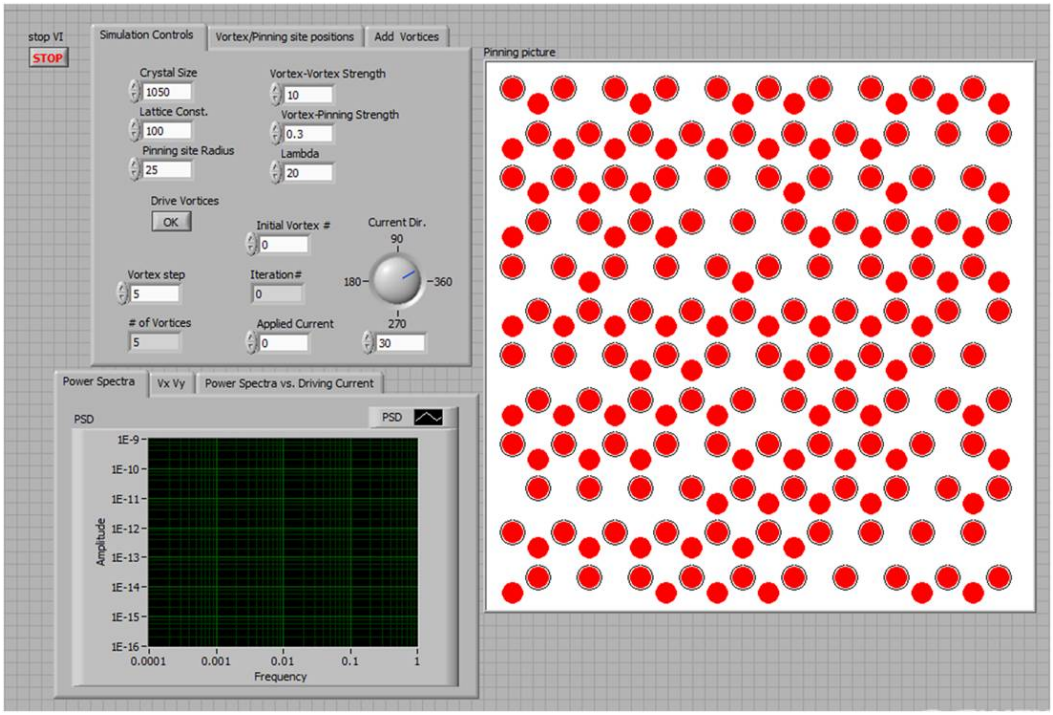

Figure A.1: LabVIEW Simulation program

Front page showing a filled triangular lattice of pinning sites (black circles) and partial filling of the interstitial lattice. This image also shows the simulation controls and the power spectrum that is collected over 10000 time steps made at each applied driving force. Driving force is controlled via the Current Dir. Knob which rotates 360 degrees.

vortex-vortex repulsion $\mathbf{f}^{v.v.}$ represented by a modified first order Bessel function K_1.

$$\mathbf{f}_i^{vv} = \sum_{j=1}^{N_v} f_0 K_1 \left(\frac{|r_i - r_j|}{\lambda} \right) \hat{\mathbf{r}}_{ij} \tag{A.2}$$

where

$$\mathbf{f}_0 = \frac{\Phi_0^2}{8\pi^2 \lambda^3} \tag{A.3}$$

and the vortex-pinning site attraction $\mathbf{f}^{vp}$

$$\mathbf{f}_i^{vp} = \sum_{k=1}^{N_p} \frac{f_p}{r_p} |r_i - r_{pk}| \, \Theta \left(\frac{r_p - |r_i - r_{pk}|}{\lambda} \right) \hat{\mathbf{r}}_{ik}^{(p)}. \tag{A.4}$$

Additionally, a driving force replicates the Lorentz force from an applied current on a vortex $\mathbf{f}_d$. A sum is taken of the individual force components to calculate the velocity felt by each vortex $\mathbf{v}_i$. Since the pinning sites are a fixed lattice, if the driving current $\mathbf{f}_d$ is applied at a different direction, the orientation of the pinning landscape changes for the simulated crystallite, thus the effect of different orientations can be simulated by simply changing the driving current direction.

The pinning array was built by defining the centers of parabolic pinning centers r_{pk} these pinning sites where given a characteristic size r_p and a pinning strength was universally defined for all of the pinning sites $\mathbf{f}_p$. The heavy-sided step function Θ was employed to define the pinning site size, and ensure that once a vortex escapes a pinning site it would feel no influence from it. The λ term in the denominators of $\mathbf{f}^{vv}, \mathbf{f}^{vp}$ acts to normalize the lengths in the simulation in terms of the penetration depth. Cutoffs are placed on vortex-vortex interactions; typically greater than 6λ and smaller than 0.1λ. These cutoffs serve to limit the range of vortices that will interact with a given vortex and prevent a divergent interaction if the vortices travel too close to each other.

One of benefit of using LabVIEW, is the ability to assign each term in the master program to a specific sub VI. In this way each component could be built and tested before joining assembling the entire master equation. This also allows users to vary terms and build different simulation programs.

The program first defines a triangular array of pinning sites given the size of the pinning site, the spacing between nearest neighbor pinning sites, and the size of the crystal being simulated. Once the pinning lattice has been defined a finite number of vortices are added to the crystal by assigning the vortices to a pinning/interstitial site. Earlier simulations used a fixed number of vortices added randomly as a group to the simulation space and underwent random x-y Langivin temperature displacements. The amplitude of these temperature displacements were slowly lowered to zero as a means to relax the vortex lattice into a triangular array. The result of the thermal annealing of the vortex lattice inevitably placed the vortices in the pinning sites. Representative plots of the array before and after using the Langevin relaxation can be seen in figure

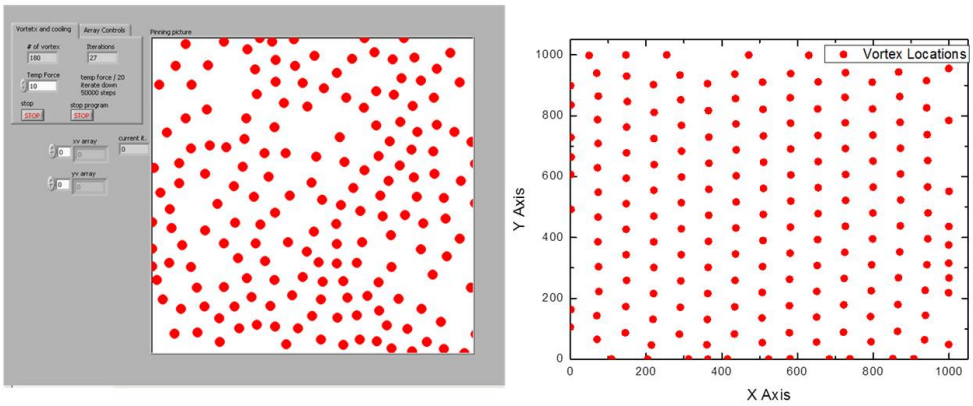

Figure A.2: "Thermal" annealing of vortex lattice

Illustration of a thermal annealing of randomly placed vortices by decreasing the amplitude of Langevin kicks. Left image shows the initial orientation of the vortices, right image shows the final orientation. Note that final orientation is essentially a triangular lattice.

A.2.

Once the vortex lattice is initialized the master equation is employed to move the vortices for a specified number of iterations (time steps). If we consider a vortex density where over half of the pinning sites are vacant and the rest of the vortices lay in the filled pinning sites. While the driving current is less than the pinning strength the vortices are trapped in the potential well. For driving currents close to the pinning strength vortices may be displaced due to the additional force provided by the vortex-vortex repulsion from neighboring pinned vortices. Eventually, once the magnitude of the driving force $\mathbf{f}_d$ exceeds the pinning strength $\mathbf{f}_p$ all vortices flow to adjacent pinning sites.

The simulated experiment is comparable to measurements made investigating the voltage vs. current characteristics of a superconductor at a fixed field/vortex density. While this is a relatively straightforward experiment to compare our results to, it does mean that a variety of different vortex densities must be run through a wide range of driving currents before any matching behavior can be seen. Because of this, it takes a considerable amount of time to complete a data run spanning multiple vortex densities

(Approximately eight hours/run for field values up to H_1, above the first matching field requires a progressively longer time which scales with the number of vortices).

The sample space is has periodic boundary conditions on all sides. Further, the edges have two constantly pinned vortices that act as a repulsive image charge of the periodic boundary. While these boundary conditions help to ensure order in the sample for vortex densities at the commensurate vortex density H_1, it is far from ideal. Above the first matching field the absence of interstitial vortices in the fixed boundary lattice results in a relaxation of the interstitial vortex lattice. Furthermore, the current boundary conditions must be modified such that when $f^d > f_p$ the boarder lattice should no longer be pinned. The effects of these limitations in the boundary conditions show themselves as the vortex density becomes larger than H_1. Thus the boundary conditions for the simulation are an area where the improvements must be made.

Even with the limitations in boundary conditions, in simulations we find some agreement with experiments if we measure the average velocity for a variety of vortex densities as a function of driving force. We find that for vortex densities below the first matching field there is an abrupt jump in the average velocity when the vortices are finally displaced from the pinning sites. Above H_1 there is a smoother transition in the vortex velocity as pinned vortices are displaced by the interstitial vortices. Both of these results are in qualitative agreement with previous molecular dynamic simulations [40, 20]. The average vortex velocity versus driving force can be seen for both high and low vortex densities in figure A.3. Additionally, if we define a threshold voltage and track the driving force at each vortex density where the average vortex velocity exceeds this threshold; we arrive at a plot much like our critical current versus field plot. Here we see that there is a strong matching feature at H_1 and a weak matching feature at H_2 as shown in figure A.4.

The data plotted in figures A.3 and A.4 illustrate that there is a matching effect that occurs at the first matching field, but the second matching field shows a much weaker response. The large suppression in depinning force is due to the much weaker caging effect from to the interstitial vortex lattice. Additionally, this response is influenced by the absence of interstitial vortices in the border surrounding the simulation space. Thus the force on the interstitial lattice is decreased as they move toward the edge of the sample space. Figure A.4 illustrates the drastically different vortex velocity vs. driving

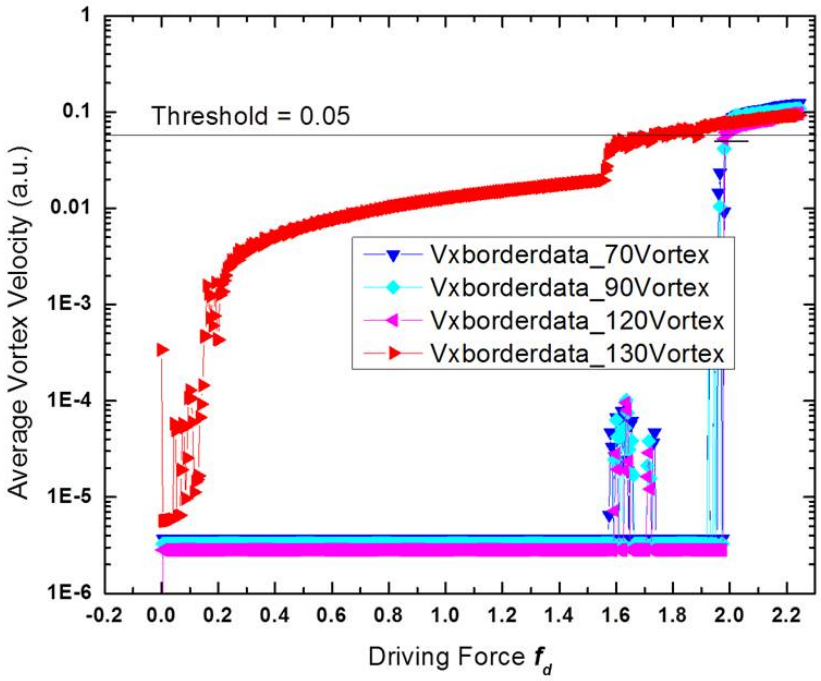

Figure A.3: Average velocity vs. driving force

Plot of average x vortex velocity versus driving force for a variety of vortex densities for a lattice with 120 pinning sites.

current for 130 vortices compared to 120. Again this is evidence of a problem that must be addressed in the current program.

A.2 Possible Improvements

The current state of the simulation is a functioning program for vortex densities up to the pinning site density. Once the vortex density exceeds the pinning site density there is a noticeable breakdown in vortex dynamics at the edges of the simulation space. Here the symmetry of the pinning potential is broken by not considering the interstitial

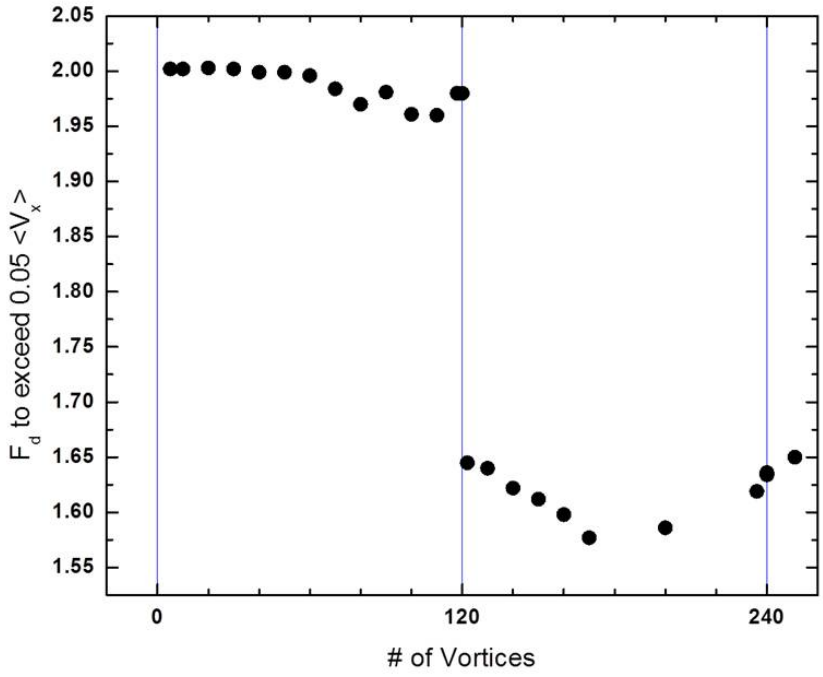

Figure A.4: Depinning force vs. vortex density

Plot of the driving force versus vortex density where the average x velocity of the vortices exceeds 0.05 in a triangular lattice with 120 pinning sites. A shard transition in driving force is observed at 120 vortices where interstitial vortices first appear.

vortices in the periodic boundary conditions or the sample border.

Two possible solutions can be imagined for this problem. If the border was changed from being a ring of occupied pinning sites to a border that is filled proportional to the vortex density of the simulation, we might expect more uniform results across the entire simulation space. Otherwise, a border that is truly periodic such that a vortex at the border feels the influence from vortices on both sides of the sample. This periodicity could possibly be invoked by assigning each vortex a periodic phase based on position. By making the simulation truly periodic, one assumes that all current edge effects should

be mitigated.

It would be ideal to modify the current code such that the time step could be adjusted. Current vortex motion occurs by taking a finite sum of all the forces acting on each vortex and using this sum to determine the new position of the vortex. Size of the time step may be artificially large and may miss certain vortex dynamics. This possibility must be investigated by examining the current time step, with smaller (fractional) time steps to see if trajectories for both time scales are identical.

Another possibility for modifying the current simulation is to solve the master equation using a more advanced differential equation technique than the current Euler method. Literature searches have suggested that employing the Runge-Kutta methods of iterative differential equation solving may be employed [41]. This would require a recasting of our current simulation but may lead to a improved calculation of the vortex motion, and should be relatively straight forward to employ.

A.3 Summary

My vortex dynamics simulation serves as a good starting point for investigating the interaction of vortices and pinning sites. There are concerns that need to be addressed regarding the boundary conditions for the simulation, however, testing the current code shows that the equations governing the motion and pinning of vortices in the sample are roughly working. The existing program could be modified to simulate different problems e.g. the pinning sites represent hard boundaries. Such modifications would allow the program to investigate restricted diffusion, jamming, anisotropic particle flows, or self-organized criticality due to particle avalanches. All such experiments require very little modification to the existing code, and most simplify the existing code to the hard particle limit which minimizes the vortex-vortex interaction.

What follows is a brief description of the relevant sub VI's that make up the simulation program.

`Vortex Init 1.vi`: Builds a periodic array of pinning sites.

`Pinning Picture.vi`: Appends information to picture used to track motion of vortices.

`2nd matching array offset.vi`: Calculates the positions to add vortices with

minimal lattice relaxation is necessary.

`Vortex adder 0-3rd.vi`: Adds vortices to the simulation filling up the commensurate then interstitial sites.

`Vortex vortex interaction 4.vi`: Calculates the force on a specific vortex from surrounding vortices out to 6λ.

`Pinning force 3.vi`: Calculates the response of a vortex trapped in a parabolic pinning site of a given radius.

`Applied Current 1.vi`: Calculates the influence of a driving current on the vortices.

`Periodic Array BC3.vi`: Wraps the vortex trajectory if it exceeds the crystal size.

`Vortex Saver.vi`: Collects and saves associated vortex data as a tab deliminated *.lvm file.

Appendix B

MFM Measurements: Two Ferromagnetic Material Sample Fabrication

This appendix describes a technique that was developed to observe the simultaneous magnetic response of two materials vs. a non-magnetic background under a Magnetic Force Microscope (MFM). While this technique was not used in the study of the superconducting samples, it was a unique process that illustrated some limitations in the quantitative signal detected by an MFM [42]. What follows is a reference, including detailed steps for replicating our two metal samples.

Our general technique, for MFM measurements consisted of observing the phase change over a magnetic material versus a non-magnetic standard (typically a bare silicon substrate). By varying the MFM lift height, the tip/sample separation is altered and a plot of phase response versus lift height can be made. A non-zero phase response is observed in ferromagnetic materials over a range of 0-300 nm [43]. Our measurements found a large variation in phase response between different samples made of the same material (Py, Co, CoFe). These results cast doubt as to what determines the magnitude of the magnetic signal.

Given the large identical-ferromagnetic-material sample to sample variation, we developed a novel sample fabrication technique to allowing two materials to be imaged in

a single scan, thus providing a way to measure the phase response of multiple materials at the same time and address the sample to sample variation. With the ability to measure two materials at once, many experiments could be conducted by exploiting the multiplicity of material options. Such as imaging two different ferromagnetic materials, two identical materials deposited at different times and both ferromagnetic and non-ferromagnetic materials together. Further, the technique might be useful to employ for the study of other metallic properties e.g. conductivity, of different metals.

The samples are made via standard optical lithography techniques employing both additive (sputter with lift-off) and subtractive (ion mill) techniques. Fabrication steps are shown in figure B.2-B.8.

The end product will be a sample with stripes of two metals lying next to each other yet ordered in columns surrounded by the insulating substrate. In this way we were able to construct films where 10-20 μm regions could be scanned diagonally such that a scan would cross the non-interacting substrate and both metals, allowing a measurement of the phases of all materials at a single time [42]. Our samples consisted of 40 nm of $Co_{90}Fe_{10}$ and either Permalloy, or Ni with a 5 nm capping layer of Ta on a silicon substrate the AFM topography of a sample is shown in [fig:MFMscan].

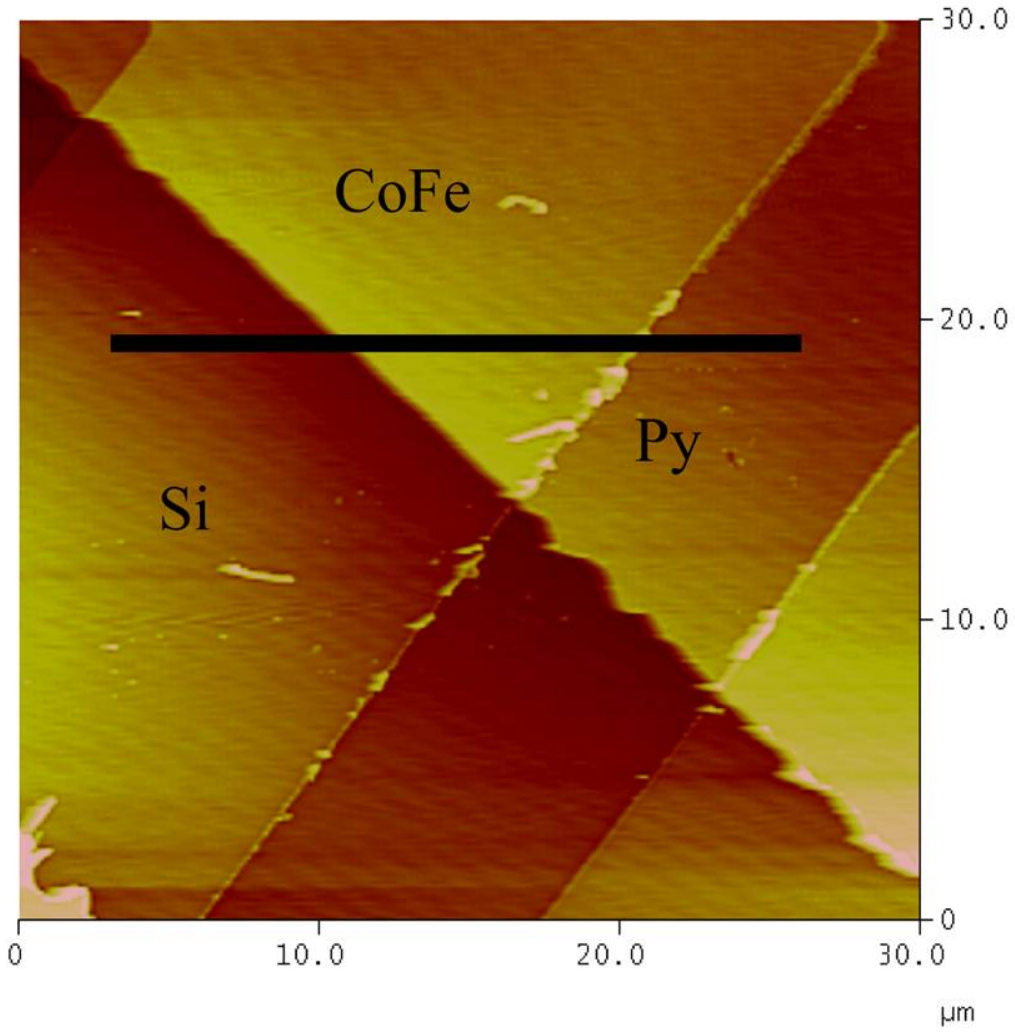

Figure B.1: AFM scan of sample

AFM scan showing the Si reference layer, the 10 μm wide Permalloy layer and the 20 μm wide CoFe layer (both materials 30 nm thick). The horizontal black line indicates the scan direction illustrating the ability to measure the phase response of both materials at the same time. Dark region in the Si section of sample is due to an over mill of the CoFe layer.

Figure B.2: Fabrication Step 1

Step 1: Metal is first deposited and capped on a cleaned Si/SiNx substrate. Material thickness is important to note as it will determine the ion mill time. Remove sample, coat with photo-resist (30 sec @ 3000 RPM, 1818 follow standard procedures for developing photo-resist).

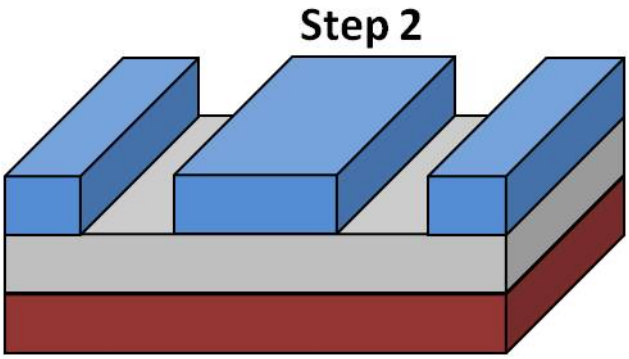

Figure B.3: Fabrication Step 2

Step 2: Use standard optical lithography techniques, expose and develop photo-resist. In this step the mask consists of long thin rectangles (10 μm in width 4 mm in length with 20 μm spacing between). The differences in width will be used to identify each of the materials deposited between the fencing effects of each material.

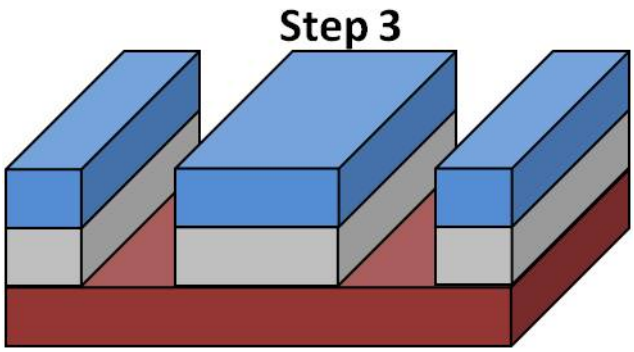

Figure B.4: Fabrication Step 3

Step 3: Load sample into ion mill. Determine mill time from film thickness and material etch rate. Photo-resist acts as a shield for material underneath. Use the mill to remove the exposed material to the sample substrate. The sample should show the underlying substrate and a metal mesa shielded by the photo-resist layer. When using the Ion mill, alternate mill time (3-4 min) with cool down time (1-2 min) to avoid overheating and burning photo-resist.

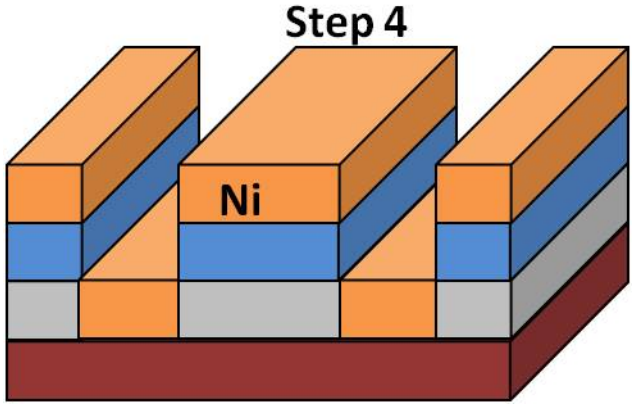

Figure B.5: Fabrication Step 4

Step 4: Return sample to vacuum chamber and deposit second layer filling up the valleys to the height of the previous layer. Cap material as necessary ~ 5 nm Ta).

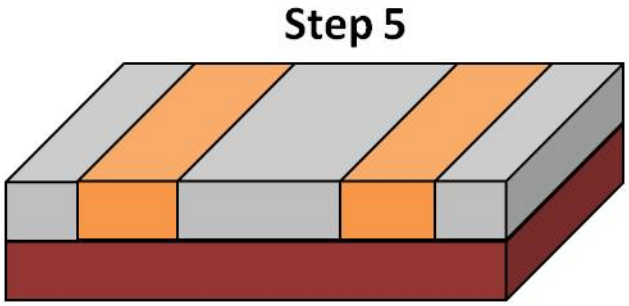

Figure B.6: Fabrication Step 5

Step 5: Perform standard lift-off of photo-resist layer using acetone and gentle sonication. Sample should now show two alternating films across the entire substrate.

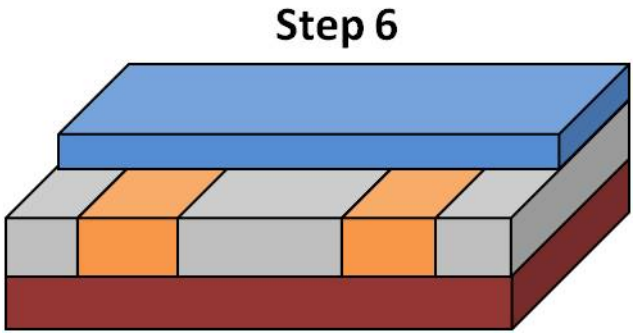

Figure B.7: Fabrication Step 6

Step 6: A second mill step is required to provide a base-line for phase measurements. Repeat the photolithography step 2 expose using the same mask except rotating orientation by 90 degrees. This will produce a cross-hatch pattern across the sample.

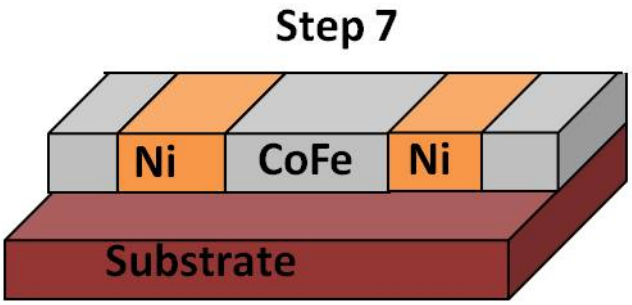

Figure B.8: Fabrication Step 7

Step 7: Use the ion mill and again etch to the substrate. With two different metals a non-uniform mill rate will occur, this is compensated by over milling the substrate to ensure no magnetic material remains.